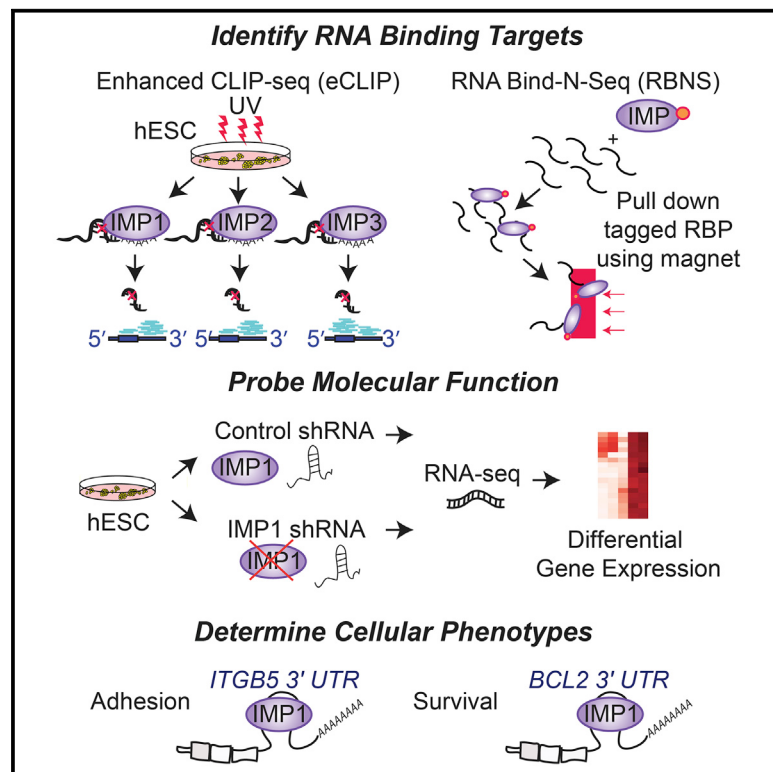


Enhanced CLIP Uncovers IMP Protein-RNA Targets in Human Pluripotent Stem Cells Important for Cell Adhesion and Survival

Graphical Abstract



Highlights

- Enhanced CLIP identifies thousands of reproducible IMP1, IMP2, and IMP3 binding sites
- IMP1 and IMP2 binding sites are highly correlated in 3' UTRs of coding genes
- Integrins represent a key mechanism for IMP1 modulation of cell adhesion in hESCs
- Apoptosis of hESCs resulting from depletion of IMP1 is mediated by IMP1 target *BCL2*

Authors

Anne E. Conway, Eric L. Van Nostrand, Gabriel A. Pratt, ..., Christopher B. Burge, D. Leanne Jones, Gene W. Yeo

Correspondence

leannejones@ucla.edu (D.L.J.), geneyeo@ucsd.edu (G.W.Y.)

In Brief

Using transcriptome-wide mapping with eCLIP, Conway et al. identify thousands of IMP1, IMP2, and IMP3 RNA binding sites in human stem cells, identifying both overlapping and distinct targets among IMP proteins. Two IMP1 targets, *ITGB5* and *BCL2*, help mediate IMP1 roles in cell adhesion and survival.

Accession Numbers

GSE78509

Enhanced CLIP Uncovers IMP Protein-RNA Targets in Human Pluripotent Stem Cells Important for Cell Adhesion and Survival

Anne E. Conway,^{1,2,3,10} Eric L. Van Nostrand,^{1,2,10} Gabriel A. Pratt,^{1,2,4} Stefan Aigner,^{1,2} Melissa L. Wilbert,^{1,2} Balaji Sundaraman,^{1,2} Peter Freese,⁵ Nicole J. Lambert,⁵ Shashank Sathe,^{1,2} Tiffany Y. Liang,^{1,2} Anthony Essex,³ Severine Landais,³ Christopher B. Burge,⁵ D. Leanne Jones,^{3,6,7,*} and Gene W. Yeo^{1,2,8,9,*}

¹Department of Cellular and Molecular Medicine, University of California at San Diego, La Jolla, CA 92037, USA

²Stem Cell Program and Institute for Genomic Medicine, University of California at San Diego, La Jolla, CA 92037, USA

³Laboratory of Genetics, Salk Institute for Biological Studies, La Jolla, CA 92037, USA

⁴Department of Bioinformatics and Systems Biology, University of California at San Diego, La Jolla, CA 92093, USA

⁵Department of Biology, Massachusetts Institute of Technology, Cambridge, MA 02142, USA

⁶Department of Molecular, Cellular and Developmental Biology, University of California at Los Angeles, Los Angeles, CA 90095, USA

⁷Eli and Edythe Broad Center of Regenerative Medicine and Stem Cell Research, University of California at Los Angeles, Los Angeles, CA 90095, USA

⁸Molecular Engineering Laboratory, A*STAR, Singapore 1190777, Singapore

⁹Department of Physiology, Yong Loo Lin School of Medicine, National University of Singapore, Singapore 1190777, Singapore

¹⁰Co-first author

*Correspondence: leannejones@ucla.edu (D.L.J.), geneyeo@ucsd.edu (G.W.Y.)

<http://dx.doi.org/10.1016/j.celrep.2016.03.052>

SUMMARY

Human pluripotent stem cells (hPSCs) require precise control of post-transcriptional RNA networks to maintain proliferation and survival. Using enhanced UV crosslinking and immunoprecipitation (eCLIP), we identify RNA targets of the IMP/IGF2BP family of RNA-binding proteins in hPSCs. At the broad region and binding site levels, IMP1 and IMP2 show reproducible binding to a large and overlapping set of 3' UTR-enriched targets. RNA Bind-N-seq applied to recombinant full-length IMP1 and IMP2 reveals CA-rich motifs that are enriched in eCLIP-defined binding sites. We observe that IMP1 loss in hPSCs recapitulates IMP1 phenotypes, including a reduction in cell adhesion and increase in cell death. For cell adhesion, we find IMP1 maintains levels of integrin mRNA specifically regulating RNA stability of *ITGB5* in hPSCs. Additionally, we show that IMP1 can be linked to hPSC survival via direct target *BCL2*. Thus, transcriptome-wide binding profiles identify hPSC targets modulating well-characterized IMP1 roles.

INTRODUCTION

Human embryonic stem cells (hESCs) are an invaluable model system to address mechanisms of early human development due to the ability to self-renew and differentiate into the majority of cell types in the mammalian embryo. Recent studies profiling RNA regulatory networks controlled by RNA binding proteins (RBPs), including RBFOX2, LIN28A, and MBNL, have demon-

strated that RBPs play key roles in maintenance of pluripotency through regulating diverse aspects of RNA processing (Han et al., 2013; Wilbert et al., 2012; Yeo et al., 2009).

The IGF2 mRNA binding proteins (IMPs/IGF2BPs) are a highly homologous family of RBPs that are conserved from insects to mammals (Hansen et al., 2004; Nielsen et al., 1999). Humans and mice have three IMPs (IMP1-3/IGF2BP1-3), which are expressed broadly during early development. Protein expression generally decreases in most tissues post-natally, with the exception of sustained expression in the germline in adults (Hammer et al., 2005; Hansen et al., 2004). IMP2 mRNA, however, remains expressed in adult murine tissues (Bell et al., 2013). IMP1 is necessary for proper embryogenesis (Hansen et al., 2004), and IMPs are upregulated in many different types of cancer including lung, liver, breast, and colon, with expression being tightly correlated with poor patient prognosis (Dimitriadis et al., 2007; Ross et al., 2001).

Molecular mechanisms of how IMP proteins bind and regulate their target RNAs have been studied predominantly in vitro. Molecules of IMP1 protein bind RNA cooperatively and sequentially, dimerizing to form a stable complex with bound RNA via the hnRNP K homology (KH) domains 1–4 (Nielsen et al., 2004). All four KH domains contribute to RNA binding and are important for localization of IMP (Nielsen et al., 2002). Furthermore, both IMP2 and IMP3 are able to heterodimerize on a target RNA with IMP1 via the four KH domains (Nielsen et al., 2004). Identification of IMP1 RNA targets in vivo revealed IMP1 modulates development and differentiation by regulating various stages of RNA processing. The namesake target of the IMP family, *IGF2*, is primarily regulated at the level of translation, but IMP1 can either promote or repress translation of *IGF2* depending on cellular context (Dai et al., 2013; Nielsen et al., 1999). IMP1 also controls the localization and translation of neuron-specific *Tau* mRNA in a

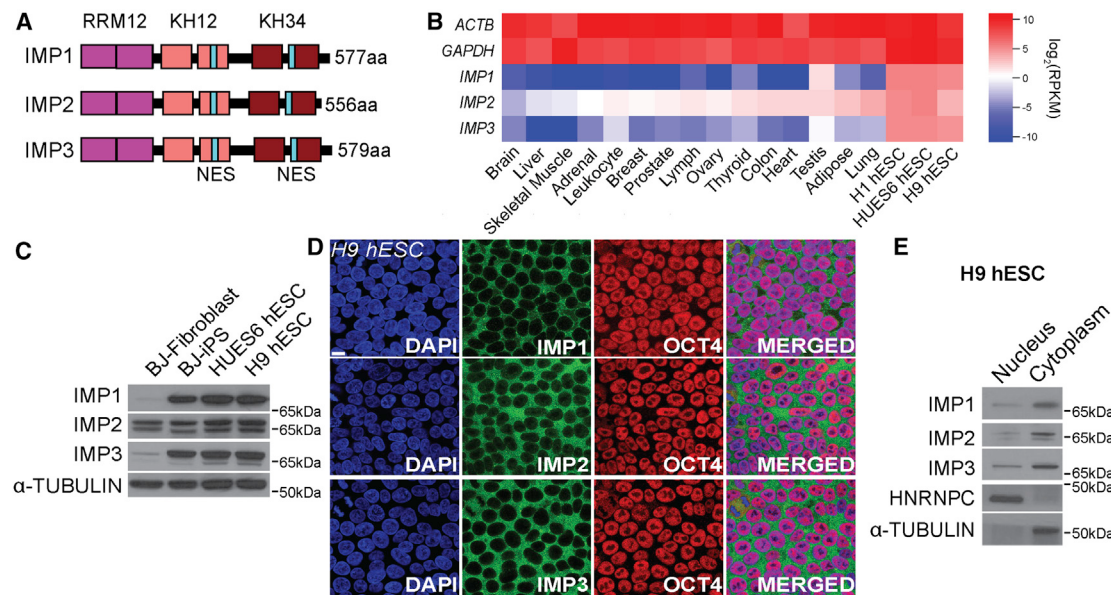


Figure 1. Expression Patterns of IMP1, IMP2, and IMP3 RNA Binding Proteins

- (A) Domain structure of IMP protein family members, with RNA-recognition motif (RRM) 1-2, hnRNPK-homology (KH) 1-2 and 3-4 domains, and nuclear export signal (NES).
- (B) Illumina Bodymap tissue RNA-seq data of *IMP1-3*, *GAPDH*, and *ACTB* mRNA expression (RPKM) in comparison to H1, H9, and HUES6 human embryonic stem cells (hESCs).
- (C) IMP protein expression in human fibroblasts, induced pluripotent (iPS), and hESCs by western blot analysis.
- (D) Immunofluorescence displaying IMP localization in hESCs. Scale bar, 10 μ m.
- (E) Cellular fractionation into nuclear and cytoplasmic expression of IMP1-3 by western blot analysis.

differentiation-dependent manner (Atlas et al., 2007) and controls stability of *MYC* RNA (Bernstein et al., 1992).

Although these studies in cell lines and model organisms have provided clues into IMP regulation of a small number of RNAs, our understanding of how the IMP-RNA target orchestra is conducted transcriptome-wide in human development is incomplete. In HEK293 cells, Hafner et al. (2010) surveyed the genome-wide binding preferences of all three IMPs overexpressed with photoactivatable-ribonucleoside-enhanced crosslinking and immunoprecipitation (PAR-CLIP) and Jönson et al. (2007) surveyed the RNAs in IMP1 RNP complexes using RNA immunoprecipitation followed by microarray (RIP-ChIP). However, whether overexpression recapitulates endogenous binding is always a concern with RBPs, and indeed it was recently shown that exogenous expression of IMP1 results in aberrant sedimentation in polysomal gradient centrifugation when compared with endogenous protein (Bell et al., 2013). Therefore, to study the normal roles of endogenous IMP proteins in hESCs, we integrated two recently developed approaches: enhanced UV cross-linking and immunoprecipitation followed by high-throughput sequencing (eCLIP) to identify the endogenous RNA targets of IMP1, IMP2, and IMP3 *in vivo*, and RNA Bind-n-seq (RBNS) to uncover the *in vitro* binding preferences of full-length IMP1 and IMP2 proteins. These approaches revealed highly overlapping binding for IMP1 and IMP2 that was distinct from IMP3, suggesting the IMP family plays both redundant and distinct functions in hPSCs. Further, loss of IMP1 leads to defects in cell survival and adhesion in hPSCs that can be partially explained through its ef-

fects on direct targets *BCL2* and *ITGB5*, respectively. Thus, profiling of endogenous IMP1 targets in hPSCs reveals insight into the pathways through which well-characterized IMP1 functions are achieved in stem cells.

RESULTS

Enhanced CLIP Identifies Targets of IMP1, IMP2, and IMP3 Proteins in Human Embryonic Stem Cells

The human IMP family of RNA binding proteins (RBPs) consists of three members (IMP1, IMP2, and IMP3) that contain two RNA recognition motifs (RRMs) and four KH domains each (Figure 1A). Previous reports have observed significant expression of all three IMP proteins in pluripotent and cancer cell lines, with expression in differentiated tissues mostly limited to IMP2 (Bell et al., 2013). Analyzing public RNA sequencing (RNA-seq) datasets (Marchetto et al., 2013), we confirmed that all three members are highly expressed at the mRNA level in PSCs relative to differentiated tissues (Figure 1B). At the protein level, we validated that IMP1, IMP2, and IMP3 are all expressed in undifferentiated human ESC lines H9 and HUES6 and an induced pluripotent stem cell (iPSC) line, whereas IMP2 is also expressed in the parental fibroblasts from which the iPSC line was generated (Figure 1C). Further, immunohistochemical staining (Figure 1D) and subcellular fractionation (Figure 1E) in H9 hESCs demonstrated dominant cytoplasmic localization of all three IMP proteins. Thus, we selected H9 hESC to identify the RNA targets of IMP proteins in pluripotent stem cells.

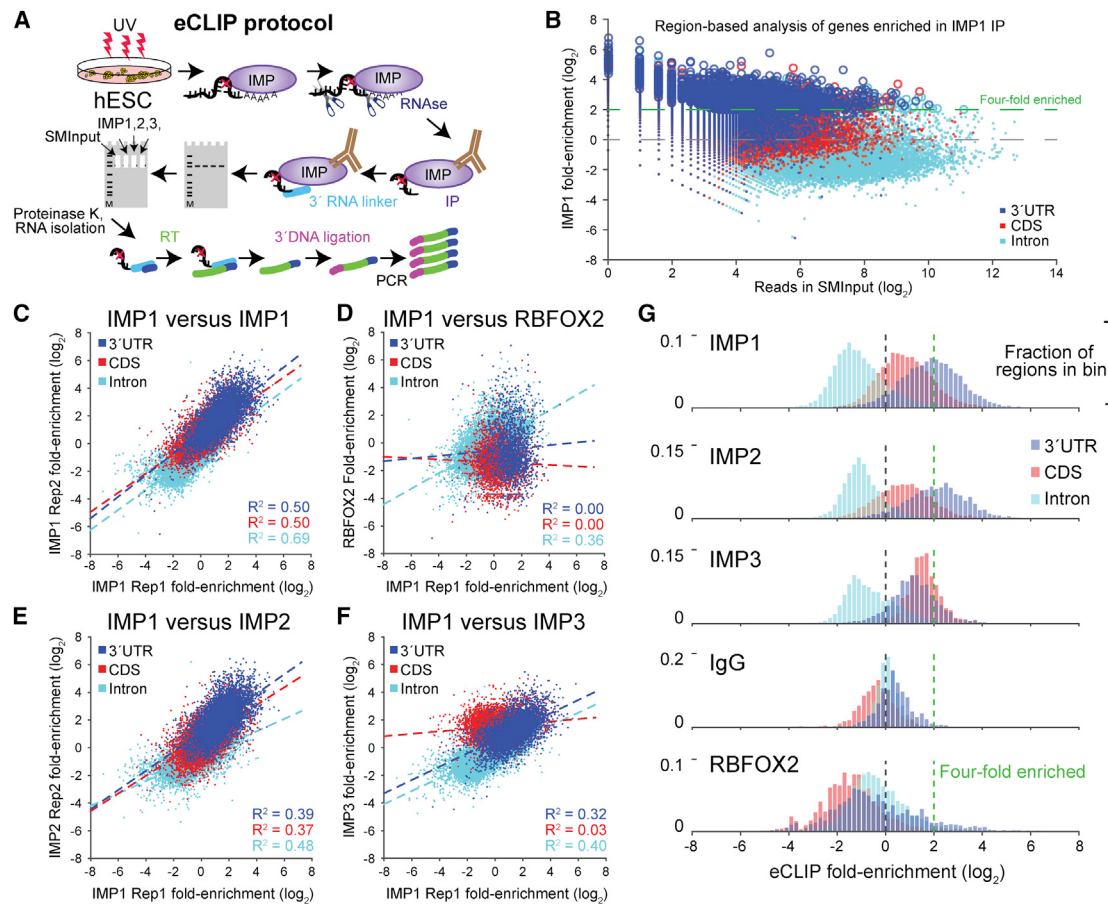


Figure 2. Identification of RNA Binding Targets of IMP1, IMP2, and IMP3 in hESCs by eCLIP

(A) Schematic of enhanced CLIP protocol. In brief, H9 hESCs were subjected to UV-mediated crosslinking, lysis, and treatment with limiting amount of RNase, followed by immunoprecipitation (IP) of protein-RNA complexes. RNA fragments protected from RNase digestion were subjected to 3' RNA linker ligation, reverse-transcription and 3' DNA linker ligation to generate eCLIP libraries for high-throughput Illumina sequencing. In addition, a size-matched input (SMInput) library was generated for each IMP protein (see the [Experimental Procedures](#) for further details).

(B) Identification of IMP1-bound regions. For each gene in Gencode v19, read density was counted separately for 3' UTR (blue), CDS (red), or introns (teal). Scatterplot indicates fold enrichment for each region in IMP1 eCLIP relative to paired SMInput (y axis), plotted against read density in SMInput (x axis). Open circles indicate significant enrichment ($p \leq 10^{-5}$ and ≥ 4 -fold) in eCLIP relative to SMInput.

(C–F) Scatter plots indicate correlation between region-based fold enrichment in eCLIP for (C) IMP1 biological replicates, (D) IMP1 versus RBFOX2, (E) IMP1 versus IMP2, and (F) IMP1 versus IMP3. For each, regions from all genes meeting a minimal read depth criteria are shown, with least-squares regression line indicated by the dotted line.

(G) Histogram of region-based fold enrichment for IMP family members IMP1, IMP2, and IMP3, unrelated splicing regulator RBFOX2, and an IgG negative control (each compared to its paired SMInput).

See also [Figures S1](#) and [S2](#) and [Tables S1](#) and [S2](#).

To uncover molecular pathways in PSCs regulated by IMP proteins, we utilized an enhanced iCLIP (eCLIP) protocol to identify transcriptome-wide RNA targets of the IMP proteins (König et al., 2011; Van Nostrand et al., 2016). Briefly, H9 hESCs were subjected to UV-mediated crosslinking, lysis, and treatment with limiting amount of RNase, followed by immunoprecipitation (IP) of protein-RNA complexes using commercially available antibodies that specifically recognize IMP1, IMP2, or IMP3 (Figures 2A and S1A). RNA fragments protected from RNase digestion by IMP protein occupancy were subjected to 3' RNA linker ligation, reverse-transcription, and 3' DNA linker ligation to generate eCLIP libraries for high-throughput Illumina sequencing. eCLIP improves these ligations to >70% efficiency,

significantly increasing the number of non-PCR duplicate reads that can be obtained after high-throughput sequencing (Van Nostrand et al., 2016). Specificity of the antibodies was evaluated by western blotting with recombinant human IMP1, IMP2, and IMP3 proteins (Figure S1A). Co-immunoprecipitation experiments in H1 hESCs demonstrate that the IMP1 and IMP2 antibodies do not enrich any of the other family members, while IMP3 appears to slightly co-immunoprecipitate IMP1 (Figure S1B).

We generated biological replicate eCLIP libraries for IMP1 and IMP2 and single replicates for IMP3, a negative control (IgG-only IP) and an unrelated RBP (RBFOX2) (Figures S1C and S1D). The improved efficiency of eCLIP enabled us to

generate a size-matched input (SMInput) library for each biological sample, in which 2% of the pre-immunoprecipitation sample was subjected to identical library generation steps including ribonuclear protein complex size-selection on nitrocellulose membranes. In total, ten eCLIP (including SMInput) libraries were sequenced to ~15 million reads, of which ~70% mapped uniquely to the human genome, and ~58%–93% of the uniquely mapped reads are distinct after accounting for PCR duplicates (Table S1).

Enrichment of IMP1 and IMP2 Binding to 3' UTRs

To identify which annotated gene regions are preferentially bound by the IMP proteins, we first evaluated the biological reproducibility of eCLIP (including SMInput) data. Read density within full-length annotated gene regions, namely coding exons (CDS), introns, and 3' UTRs, were highly correlated across replicates for the IMP proteins (R^2 values of ~0.9; Figures S2A and S2B), as well as between IMP proteins and their individually paired SMInput (R^2 values of ~0.7; an example IMP1 replicate is shown in Figure S2C) and IgG (R^2 values of ~0.5; example IMP1 replicate shown in Figure S2D). These high correlations were expected due to intrinsic biological biases in gene expression and shared technical variations in shearing and amplification. Therefore, as a more accurate measure of enrichment (signal) over background, we computed the fold enrichment in the IP in comparison to the paired SMInput within each region (Figures 2B and S2E–S2H; Table S2). Biological replicates of IMP1 and IMP2 showed significant correlation in fold enrichment ($R^2 > 0.46$) (Figures 2C and S2I). In contrast, neither IMP1 nor IMP2 showed correlation of binding signal at CDS or 3' UTRs with either IgG or unrelated RBP RBFOX2 (all $R^2 < 0.04$; Figures 2D and S2J–S2L).

The region fold enrichments between the paralogs IMP1 and IMP2 were also highly correlated ($R^2 > 0.37$; Figures 2E and S2M). Unexpectedly, despite having the same domain architecture and cytoplasmic localization as IMP1 and IMP2, IMP3 binding within coding exon regions was not correlated with either IMP1 or IMP2 ($R^2 \leq 0.03$; Figures 2F and S2N). Furthermore, we observed that rather than interacting with a specific limited set of RNA substrates, there was widespread enrichment in binding to particular regions within genes, as 3' UTRs were enriched for IMP1 and IMP2 binding by 2.7- to 4.4-fold (median values) above SMInput IP (Figures 2B, 2G, and S2E). This was notably higher than coding exons, which were enriched by only 1.2- to 1.7-fold. Analysis of IMP3 binding revealed an opposite trend, as coding exons were 2.9-fold-enriched while 3' UTRs were only 2.3-fold-enriched (Figures 2G and S2F). Consistent with their cytoplasmic localization, depletion of intronic signal globally across all introns was observed for all three IMP family members (depleted 1.9- and 2.3-fold for IMP1, 1.8- and 2.1-fold for IMP2, and 1.7-fold for IMP3, respectively) (Figures 2B, 2G, and S2E–S2H). These global enrichments for coding exons (depleted in both) or 3' UTRs were not observed for IgG or RBFOX2 (1.3-fold-enriched in IgG, depleted in RBFOX2). We conclude that the IMP1 and IMP2 proteins exhibit remarkably similar binding preferences to 3' UTRs of mature mRNAs, and IMP3 binding is enriched for coding exons.

Discovery of Reproducible IMP1 and IMP2 Binding Sites by Input Normalization

Due to their similarity in 3' UTR preferences, we chose to continue evaluating IMP1 and IMP2. To identify high resolution IMP1 and IMP2 binding sites, standard CLIP-seq cluster discovery was performed using CLIPper (Lovci et al., 2013). We identified 62,784 and 95,577 clusters for two biological replicates of IMP1 and 57,648 and 66,928 clusters for IMP2 replicates, with cluster sizes 36–40 bases on average (Figures 3A and S3A; Table S1). Next, as SMInput normalization significantly improves signal-to-noise in identifying true binding sites (Van Nostrand et al., 2016), we compared the read density in IP and SMInput within clusters to compute the enrichment of each cluster above SMInput (Figure S3B). As in the regional comparisons, fold enrichment at the cluster level exhibited high correlation across biological replicates (R values 0.54 and 0.51 for IMP1 and IMP2, respectively), whereas low correlation was observed when IMP1 (or IMP2) was compared to IgG or RBFOX2 (Figures S3C–S3F). Additionally, ranking clusters by fold enrichment makes them amenable to irreproducible discovery rate (IDR) analysis, a standard metric to evaluate the reproducibility of binding sites across biological replicates (Li et al., 2011). We observed that IMP1–IMP1 or IMP2–IMP2 comparisons yielded thousands of reproducible clusters at a 0.01 IDR threshold (where 1% of peaks do not reproduce), whereas identical comparisons with IgG or RBFOX2 yielded less than ten reproducible clusters (Figure 3B). These orthogonal computational approaches indicate that eCLIP of IMP1 and IMP2 yield highly reproducible binding at both the cluster and read-density-within-cluster levels.

For further analysis, we identified a set of 1,884 and 7,004 high-confidence peaks in IMP1 and 1,572 and 4,494 in IMP2 that meet stringent enrichment criteria ($p \leq 10^{-5}$ and ≥ 8 -fold-enriched versus SMInput) (Figures 3A and S3A). In contrast, IgG eCLIP identified only 142 clusters that satisfy these criteria. These stringent binding sites were highly reproducible, as over 66% of stringent clusters identified in the first biological replicate overlapped clusters in the second for both IMP1 and IMP2 (Figures 3A and S3A). Consistent with our regional analyses, IMP1 and IMP2 binding sites were generally located within the 3' UTR and to a lesser extent, within coding exons (Figures 3C, S3I, and S3J). Thus eCLIP identifies thousands of highly confident and reproducible IMP1 and IMP2 binding sites.

High-Resolution IMP1 and IMP2 Binding Is Highly Correlated

As we observed substantial correlation between IMP1 and IMP2 binding at the region level, we next compared IMP1 and IMP2 at the binding site level. Pairwise comparisons indicated 2,495 and 4,301 peaks (at the 0.01 IDR threshold), on par with that observed for biological replicates (Figure 3B). We further observed high correlation of input-normalized signal intensity ($R = 0.42$ and 0.47 for $\text{IMP1}_{\text{Rep1}}$ versus $\text{IMP2}_{\text{Rep2}}$ and $\text{IMP1}_{\text{Rep2}}$ versus $\text{IMP2}_{\text{Rep1}}$, respectively), indicating that the association of IMP1 and IMP2 is highly similar across thousands of binding sites (Figures S3G and S3H). To test whether these factors were associating to the same short regions or simply binding nearby each other, we next considered the distribution of read intensity around peak centers. Considering a window of 600-nt

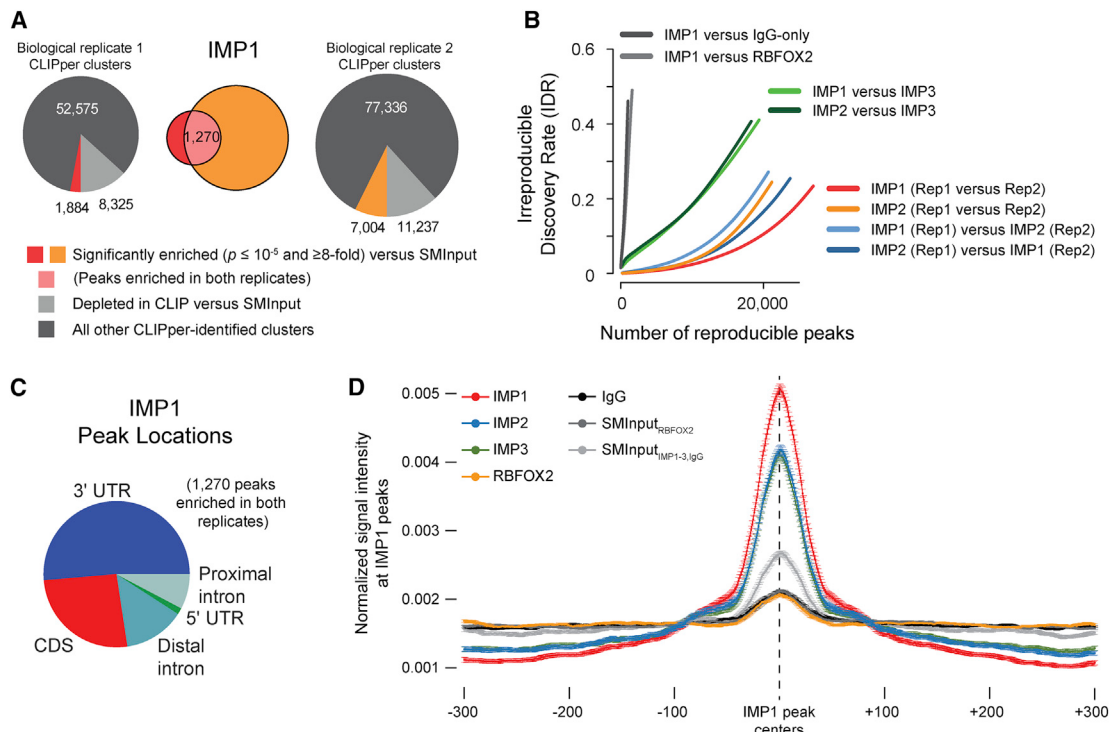


Figure 3. Reproducible Peaks Reveal Correlated Binding of IMP1 and IMP2

(A) Clusters of enriched read density within IMP1 eCLIP are identified for each biological replicate by CLIPper (gray). Comparison of cluster read density in eCLIP and paired SMIinput identifies a subset of clusters enriched above SMIinput (red/orange; also see Figure S3B), which show high overlap between replicates (center). See Figure S3A for IMP2.

(B) Irreproducible discovery rate (IDR) analysis comparing peak fold enrichment across various datasets are indicated. Rep1 was used unless otherwise indicated.

(C) Pie chart indicates the distribution of significantly enriched IMP1 peak locations across the transcriptome for replicating peaks described in (A). See Figure S3I for all (including non-significant) IMP1-enriched clusters and Figure S3J for IMP2.

(D) Plot indicates the normalized read density for indicated eCLIP experiments (Rep2 for IMP1 and IMP2), centered around the midpoint of significantly enriched IMP1 peaks (described in A) identified from an independent biological replicate (Rep1). Read densities across each peak region were normalized within the 600 nt window, and mean (points) and SEM (error bars) were calculated across all peaks for both eCLIP and paired SMIinput datasets as indicated. See also Figure S3 and Table S2.

centered on the midpoint of IMP1 peaks from an independent biological replicate, we observed that both IMP1 and IMP2 read density are enriched at the peak centers (Figure 3D). Thus, despite the IMP1 and IMP2 antibodies showing very little cross-immunoprecipitation (Figure S1B), analysis of our eCLIP data at both the region- and cluster-level indicates that IMP1 and IMP2 binding signals are as highly correlated as biological replicates of IMP1 or IMP2.

RNA Bind-N-Seq Identifies CA-Rich Motifs Enriched in Coding and 3' UTR Binding Sites

To characterize the sequence specificity of IMP proteins, we applied RNA Bind-N-seq (RBNS) (Lambert et al., 2014) to purified full-length human IMP1 and IMP2. After incubation of protein with randomized RNA pools, affinity purification, and high-throughput sequencing, we performed motif analysis to calculate enrichment over input (R) values (Figures 4A, S4A, and S4B). This identified two CA-rich motifs for each IMP: a primary motif exemplified by AY(A)1YA and secondary motif exemplified by Y(A)2YA (Figures 4B and 4C), with many enriched 6-mers

(52% for IMP1, 49% for IMP2) containing one of four 4-mers (CACA, UACA, AACCA, CAUA), similar to previously identified IMP motifs (Alipanahi et al., 2015; Hafner et al., 2010; Ray et al., 2013). We observed a high correlation between IMP1 and IMP2 6-mer enrichments ($R^2 = 0.788$) (Figure 4D), whereas IMP1 and RBFOX2 were uncorrelated ($R^2 = 0.018$) (Figure 4E), indicating that the RBNS assay captured IMP-specific binding signatures.

Next, we interrogated whether hESC IMP binding sites identified by eCLIP were enriched for the RBNS-identified *in vitro* motifs. We found that hexamers containing the CACA core sequence were shifted toward higher IMP1 RBNS enrichments, and they also showed greater enrichments among IMP1 eCLIP 3' UTR and CDS binding sites than other hexamers (Figures 4F and S4C). Other RBNS motifs (UACA, AACCA, CAUA) showed more variable enrichment, suggesting a distinguishable difference between *in vitro* and *in vivo* binding preferences (Figures 4F–4H). The enrichment for the CACA motif was more significant when using the subset of stringent CLIP-enriched peaks, consistent with these peaks having improved signal-to-noise

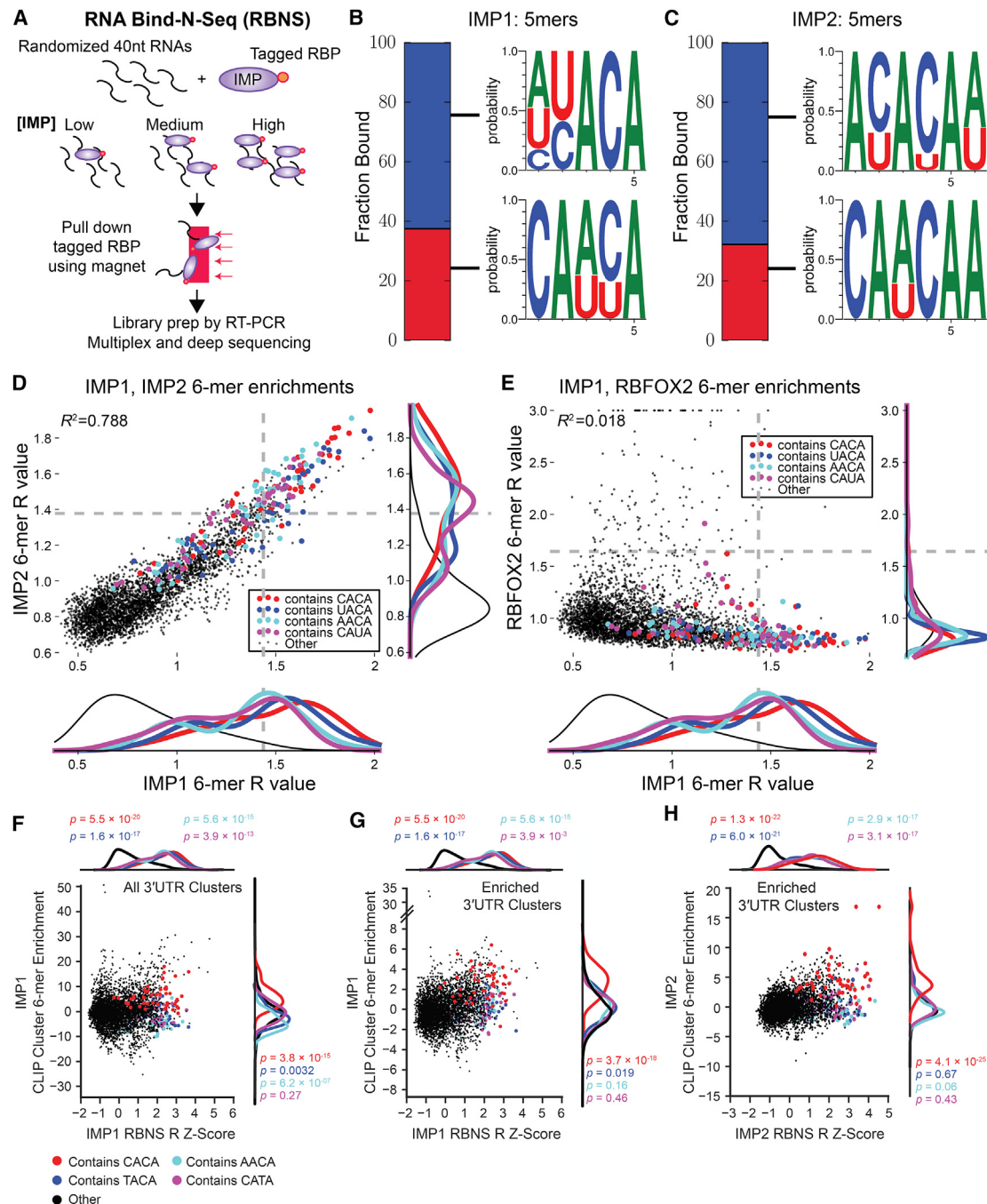


Figure 4. RNA Bind-N-Seq Identifies an AC-Rich Preference for IMP1 and IMP2 Binding

(A) Schematic of RNA Bind-N-seq (RBNS) protocol.

(B and C) Motif logos with corresponding probability bar graphs made from aligning enriched 5-mers for IMP1 (B) and IMP2 (C). All 5-mers with an enrichment Z score ≥ 2 with two or fewer mismatches to the most-enriched 5-mer were aligned to create top logo; remaining 5-mers with enrichment Z score ≥ 2 were aligned to create bottom logo. Probabilities in left bar graph are proportional to the summed enrichments of all 5-mers aligned in each logo.

(D and E) Comparison of 6-mer enrichments (RBNS R values) in IMP2 (D) or RBFOX2 (E) versus IMP1. 6-mers containing one of the top four non-overlapping IMP1 4-mers are colored, and significant enrichment (Z score ≥ 2) is indicated by dotted lines.

(F–H) Comparison of RBNS and eCLIP k-mer enrichment. 6-mers containing a CACA 4-mer (red), TACA 4-mer (navy), AACCA 4-mer (light blue), and TACA 4-mer (magenta) are highlighted. (F–G) IMP1 RBNS enrichment of all 6-mers (x axis) is plotted against (F) enrichment in all reproducible eCLIP 3' UTR clusters, or (G) stringent reproducible 3' UTR peaks only (as described in Figure 3A). (H) IMP2 RBNS enrichment plotted against motif enrichment in IMP2 stringent eCLIP clusters.

See also Figure S4.

(Figures 4G and S4D). IMP2 showed similar enrichment for CA-rich sequences in both RBNS and eCLIP binding sites (Figure 4H). Thus, these results demonstrate that IMP1 and IMP2 interact with CA-rich sequences in vitro, and this preference can be observed for coding and 3' UTR binding sites in vivo.

Integrated IMP1 eCLIP and RNA-Seq Data Implicates Integrin mRNAs in IMP1-Mediated Cell Adhesion Defects

Next, we utilized our IMP1 binding data to provide insight into the direct regulatory roles of IMP1. To evaluate if loss of IMP1 affected mRNA expression, IMP1 was depleted in H9 hESCs using lentiviral transduction of independent short-hairpin RNAs (shRNAs) that specifically target IMP1 (hereafter referred to as IMP1 knockdown [IMP1^{KD}] cells) (Figures S5A and S5B). Total RNA was extracted from three biologically independent transductions of IMP1 shRNA and two transductions of a non-targeting shRNA to generate RNA-seq libraries, which were then sequenced (Figure S5C). Of the 17,013 expressed genes analyzed, we identified 257 decreased and 467 increased genes with significantly altered expression (≥ 2 -fold and $p \leq 0.05$ versus non-targeting control) upon IMP1 depletion (Figure S5D). When we compared global IMP1 RNA targets to genes affected by IMP1 depletion, we did not observe any meaningful correlation between genes that were bound and trends in gene expression changes (Figure S5E).

Nevertheless, when we considered the most CLIP-enriched 3' UTRs for IMP1, we observed significant enrichment for genes involved in cell-cell and cell-extracellular matrix (ECM) adhesion (Figure 5A). As IMP1 regulation of cell adhesion has been well characterized in cancer cell-lines (Gu et al., 2012; Vikesaa et al., 2006), we performed a quantitative crystal violet adherence assay following IMP1 depletion to determine whether loss of IMP1 affected adhesion in H9 hESCs. We found that IMP1^{KD} cells showed significantly decreased adherence compared to control shRNA-treated cells ($p < 0.05$), even within the first hour after plating, indicating that cell adhesion is also affected by loss of IMP1 in hESCs (Figures 5B–5D). We also observed that the actin cytoskeleton and cytoskeletal organization appeared disrupted upon IMP1 depletion (Figures S5F and S5G). However, analysis of our RNA-seq data did not indicate altered RNA levels of known IMP1 targets previously shown to modulate cell adhesion, such as *CTNNB1* (in breast cancer cells) (Gu et al., 2008) or *CD44* (in adenocarcinoma cells) (Vikesaa et al., 2006). In particular, despite having enriched IMP 3' UTR binding (Figure S5H), we could observe no mRNA or protein change for *CTNNB1* in IMP1^{KD} cells (Figure S5I). Similarly, although the F-actin anchoring, cell adhesion protein vinculin (VCL) was one of the most enriched genes in our eCLIP dataset (over 20-fold-enriched relative to SMInput), VCL did not appear to be affected at the RNA or protein level upon loss of IMP1 (Figures S5J and S5K). Thus, we observe cell adhesion defects as a consequence of IMP1 depletion in hESCs, but the phenotype cannot be explained simply by regulation through previously characterized IMP1 targets.

Given that IMP1 binding alone was insufficient to predict mRNA level effects, we next focused on IMP1 target genes that harbored enriched binding sites in the 3' UTR and whose

levels were also affected in the IMP1^{KD} RNA-seq data. Surprisingly, we observed that multiple genes in the integrin family were bound by IMP1 and were downregulated upon depletion of IMP1 (Figures 5E and 5F). Integrins are known to have significant roles in extracellular signaling and cell adhesion across various systems, with *ITGB5* and *ITGB1* specifically described to play key roles in human stem cell maintenance and cell adhesion (Braam et al., 2008). Interestingly, *ITGB5* was the most downregulated of all of the integrin genes and contained regions of enriched read density within the 3' UTR compared to SMInput or *RBFOX2* (Figure 5G). We performed RNA immunoprecipitation (RIP) followed by RT-PCR in an independent hESC line (HUES6) and observed IMP1 enrichment on *ITGB5*, with *ACTB* mRNA as a positive control (Ross et al., 1997) (Figure 5H), validating the interaction between IMP1 and *ITGB5* mRNA. Additionally, we confirmed downregulation of *ITGB5* and *ITGB1* mRNAs in IMP1^{KD} cells using two independent shRNAs (Figure 5I) and further observed significant depletion of ITGB5 protein upon IMP1 loss (Figure 5J).

Next, we considered potential mechanisms for IMP1 regulation of *ITGB5*. To test whether IMP1 affects *ITGB5* mRNA levels post-transcriptionally at the level of mRNA turnover, we treated hESCs with actinomycin D (ActD) to inhibit the transcription of newly transcribed RNA and collected total RNA after 60 and 120 min. Quantification of mRNA levels by qRT-PCR revealed that *ITGB5* was destabilized more quickly in the IMP1^{KD} cells compared to cells treated with a control shRNA (Figure 5K). Interestingly, *ITGB1* did not show this destabilization upon IMP1 depletion (Figure S5L), confirming specificity of this approach and indicating that IMP1 may regulate various integrins differently. Taken together, these results indicate that the well-characterized role of IMP1 in maintaining proper cell-cell interactions is conserved in hESCs, but that the downstream effectors in hESCs include unanticipated integrin targets like *ITGB5*, which is regulated at the level of mRNA turnover.

IMP1 Target BCL2 Enhances Survival of IMP1-Depleted hESCs

In addition to cytoskeletal defects, depletion of IMP1 also led to a drastic reduction in hESC colony size (Figure 6A). Embryoid bodies derived from IMP1^{KD} cells were substantially and consistently smaller than those derived from controls (Figure S6A). In order to determine whether depletion of IMP1 led to a decrease in proliferation, which could explain a decrease in colony size, we performed fluorescence-activated cell sorting (FACS) analysis using the proliferation antigen KI-67. We observed only a slight, but insignificant, difference between IMP1-depleted and control cells using two independent shRNAs targeting IMP1 (Figure S6B). To further analyze a potential role for IMP1 in hESC proliferation, cell-cycle analysis was conducted by BrdU and propidium iodide (PI) staining followed by FACS. IMP1^{KD} cells exhibited a moderate, but significant decrease in the S phase population ($p < 0.01$), along with an increase in the number of cells in G2 ($p < 0.05$) (Figure S6C). Supporting the hypothesis that a loss of IMP1 leads to an increase in cell death, we detected a statistically significant increase in Annexin V-positive IMP1^{KD} cells compared to controls by FACS ($p < 0.05$) (Figure 6B).

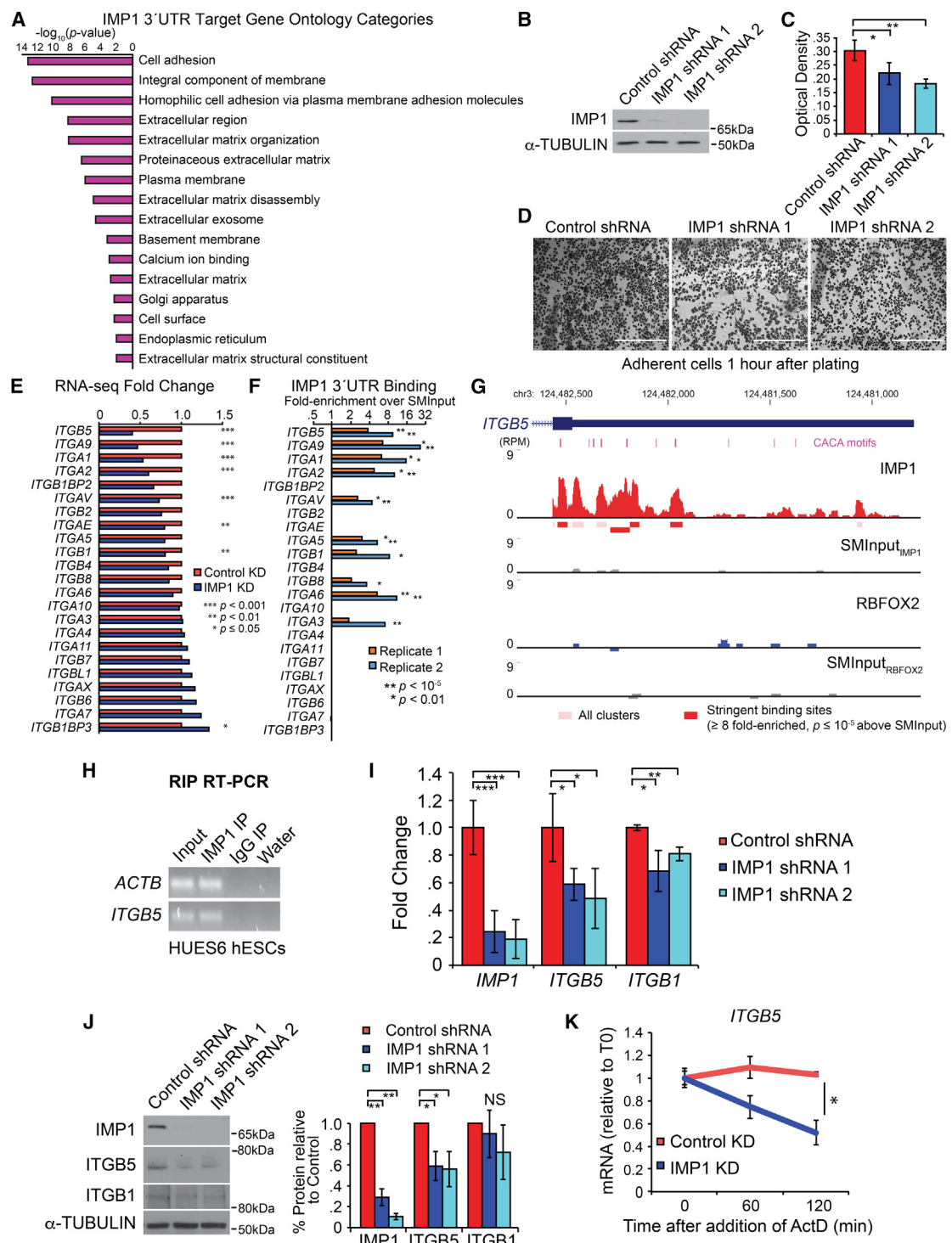


Figure 5. IMP1 Controls Integrin RNA Stability and Cell Adhesion in hESC

(A) Gene ontology analysis of genes with significantly enriched IMP1 binding in their 3' UTR in both replicates.

(B) Western blot displaying levels of IMP1 depletion in the cell-adhesion assay.

(C and D) Quantification (C) and phase contrast images (D) of H9 hESCs stained with crystal violet 1 hr after plating. Scale bar represents 400 μ m. Data are shown as mean \pm SD.

(E) RNA-seq analysis of integrin RNA expression changes following loss of IMP1 in hESC.

(F) eCLIP 3' UTR binding (\log_2 fold enrichment over SMInput) for the integrins shown in (E).

(legend continued on next page)

Additionally, we observed a significant increase in levels of cleaved-Caspase 3 upon reduction of IMP1, but not in control-treated hESCs (Figure 6C). Together, these results strongly indicate that IMP1 plays an important role in hPSC survival.

To determine the molecular mechanism by which IMP1 impacts hESC survival, we examined anti-apoptotic factors in our IMP1^{KD} RNA-seq data as candidate targets of IMP1 and found that *BCL2* (B cell lymphoma 2) was decreased by 2-fold (Table S4). This decrease in *BCL2* was confirmed at the mRNA level by qRT-PCR (Figure 6D) and at the protein level by western blot analysis (Figures 6C and S6D). Interestingly, the *BCL2* 3' UTR contains CA-rich sequences (Figure S6E) and was >2-fold-enriched over SMIinput in both IMP1 eCLIP datasets; however, *BCL2* fell below our standard significance cutoffs due to low RNA expression (Table S2). Nevertheless, we confirmed IMP1 binding by performing RIP followed by RT-PCR in HUES6 hESCs (Figure 6E). To further investigate IMP binding preferences to CA-rich sequences, as previously shown by RBNS, we performed an electrophoretic mobility shift assay (EMSA) with full-length recombinant human IMP1 protein and both wild-type (WT) and mutated versions of the *BCL2* 3' UTR (88 bp segments, see Experimental Procedures). The wild-type *ACTB* zipcode (IMP binding site) and a truncated *ACTB* zipcode were used as positive and negative controls, respectively. We were able to detect an interaction between IMP1 and the wild-type *BCL2* 3' UTR in vitro using 200 nM recombinant IMP1 protein (Figure 6F). Upon mutation of the CACA motif to GAGA, the binding affinity was dramatically reduced, indicating that IMP1 interacts specifically with the CA-rich motif that constitutes an IMP1 binding site within *BCL2* 3' UTR. Finally, to evaluate whether restoring levels of *BCL2* can suppress cell death as a consequence of IMP1 depletion, we utilized a doxycycline-inducible lentiviral system (Ardehali et al., 2011) to ectopically express *BCL2* in IMP1^{KD} hESCs. Using the Caspase-Glo assay we measured apoptosis following a titration of *BCL2* overexpression with doxycycline and found that *BCL2* is able to rescue the IMP1^{KD} cell death phenotype (Figures 6G, S6F, and S6G). Therefore, our data indicate that one pro-survival function of IMP1 in hESCs is to maintain adequate levels of *BCL2* mRNA and, consequently, maintain its anti-apoptotic activity.

DISCUSSION

Using systematic, transcriptome-wide mapping with eCLIP, we identified thousands of IMP1, IMP2, and IMP3 binding sites within RNA targets in hESCs. IMP1 and IMP3 are typically viewed as the most related family members, with greater similarity at the protein sequence level (Nielsen et al., 1999), expression patterns across

tissues and development (Bell et al., 2013) and co-immunoprecipitation during CLIP (Figure S1B), whereas IMP2 has been associated with more distinct roles, such as in metabolism (Dai et al., 2011, 2015; Janiszewska et al., 2012). Thus, hESCs (that express IMP1, IMP2, and IMP3) present a unique opportunity to observe redundant or co-regulation of RNA targets by multiple IMP family members. Surprisingly, we observed substantial overlap between IMP1 and IMP2 binding that was not observed between IMP1 and IMP3, indicating it is not simply an artifact of analyzing cytoplasmic factors with CLIP. Despite the large number of IMP1-bound mRNAs and quite dramatic phenotypes upon knockdown of IMP1 in hESCs, we observed relatively few transcripts strongly bound by IMP1 to be altered when RNA-seq was performed in hESCs depleted of IMP1. In contrast, previous studies in HEK293 cells observed a small but significant shift toward decreased expression (presumably by decreased RNA stability) of IMP targets when all three IMP proteins were simultaneously depleted (Hafner et al., 2010). These results suggest that IMP family members may share redundant regulatory roles, particularly during development and in cancer when multiple family members are expressed at high levels. The distinct binding to CDS regions observed for IMP3 suggests that further studies may yet reveal additional regulatory roles distinct from IMP1, although the severe phenotypes observed upon individual knockdown by shRNA of IMP1 and IMP2 presents a challenge to detailed characterization of redundancy among IMP family members in hESCs.

At the region-level, we observed significant IMP1 binding to a substantial fraction of all 3' UTRs. Although such widespread binding has been described for core RNA processing factors, such as the nonsense-mediated decay regulator UPF1 (Lee et al., 2015), previous studies of IMP have largely focused on a small number of specific targets. Although the degree of widespread binding is unexpected, it may help to explain why detailed studies of individual IMP targets have not identified one specific mechanism or pathway of regulation; rather, IMP binding has been shown to participate in a broad range of RNA processing regulation steps, including mRNA stability (Leeds et al., 1997), mRNA localization (Atlas et al., 2007; Ross et al., 1997), both inhibition of and enhancement of translation (Dai et al., 2011; Nielsen et al., 1999), and even potentially nuclear export (Hüttelmaier et al., 2005; Wu et al., 2015). Thus, considering IMPs as broad regulators may provide insight into how these factors can achieve these various roles. Future work will be needed to better characterize how different IMP targets are directed toward distinct regulatory mechanisms.

Although standard UV₂₅₄ crosslinking provides specificity by requiring interacting molecules to have reactive groups within one bond length apart (Wagenmakers et al., 1980), the frequency

(G) Read density tracks show read density for IMP1 (Rep2; red), RBFOX2 (blue), and paired SMIinputs (gray) across the 3' UTR of *ITGB5*. Clusters are indicated as boxes below tracks, with significantly enriched peaks indicated as darkly colored boxes.

(H) RNA immunoprecipitation for *ITGB5* in HUES6 hESCs. *ACTB* is shown as a positive control.

(I) qRT-PCR validation of *ITGB1* and *ITGB5* expression changes by RNA-seq, normalized to *HMB5*, *GAPDH*, and *18s* (error bars represent mean ± SEM, n = 3).

(J) *ITGB1* and *ITGB5* protein levels following depletion of IMP1 in H9 hESCs. An average of three independent experiments quantified by densitometry is shown on the right (replicates are normalized to the corresponding β -tubulin sample).

(K) Actinomycin D RNA stability assay. Expression of *ITGB5* was measured by qRT-PCR at different time points following addition of 10 μ M actinomycin D in H9 hESCs and normalized to *PPIA* and *RPLP0*, genes determined not to change over the given time period (error bars represent mean ± SEM, n = 3; a single asterisk indicates significance of p < 0.05 by unpaired t test).

See also Figure S5 and Tables S3 and S4.

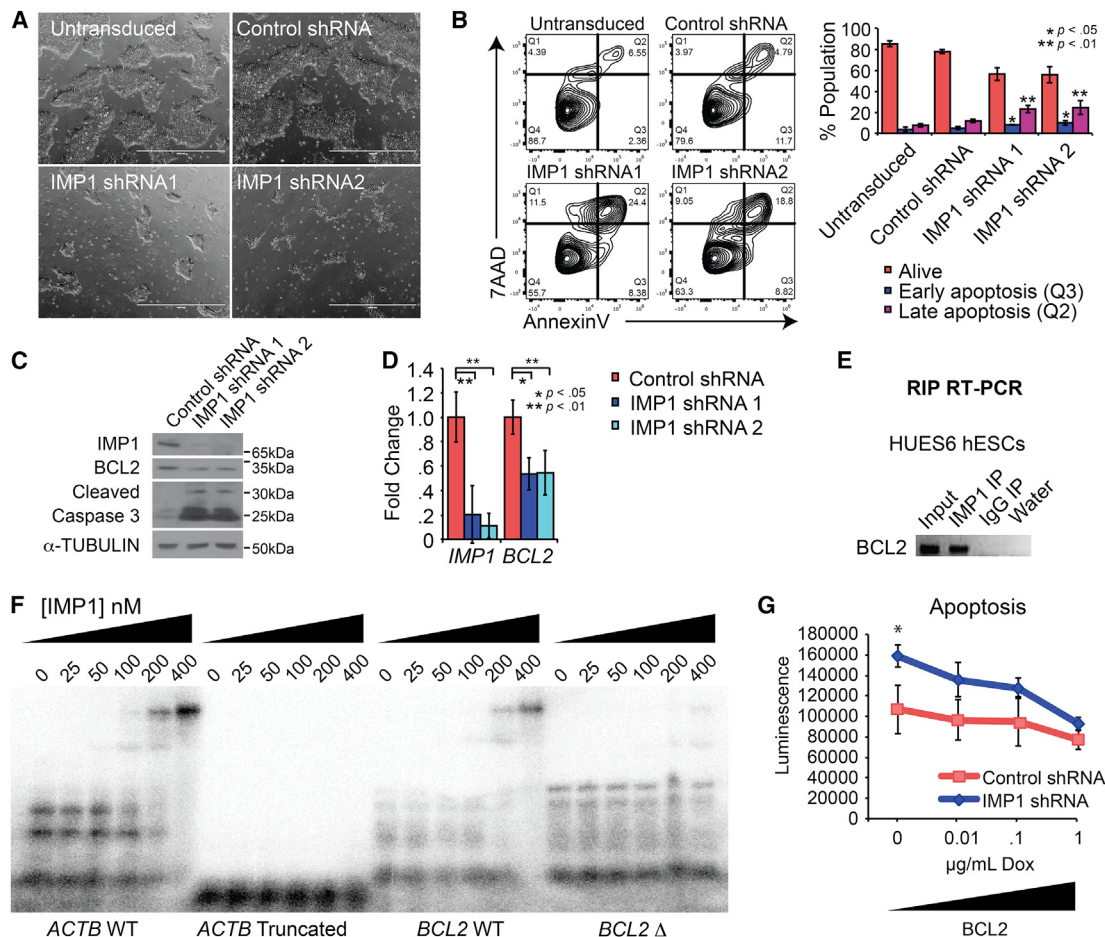


Figure 6. IMP1 Promotes Cell Survival through Regulation of BCL2

- (A) Phase contrast images of H9 hESCs following depletion of IMP1. Scale bar, 1 mm.
- (B) Shown is a representative image of flow cytometry analysis and quantification of Annexin V expression following depletion of IMP1 (error bars represent mean \pm SD, $n = 3$).
- (C) Cleaved-caspase 3 and BCL2 protein expression following depletion of IMP1 in H9 hESCs by western blot.
- (D) qRT-PCR validation of BCL2 expression following depletion of IMP1, with expression normalized to average of HMBS, GAPDH, and 18s (error bars represent mean \pm SEM, $n = 3$).
- (E) RNA immunoprecipitation (RIP) for BCL2 in HUES6 hESCs using antibodies that target either IMP1 or IgG.
- (F) EMSA results depicting IMP1 binding preferences for ACTB WT, ACTB truncated, BCL2 WT, and BCL2Δ RNAs. One representative experiment is shown.
- (G) Caspase-Glo apoptosis assay. BCL2 protein was induced with increasing amounts of doxycycline after which apoptosis was measured via luminescence using the Caspase-Glo 3/7 assay. A single asterisk indicates significance of $p < 0.05$, and two asterisks indicate significance of $p < 0.01$, determined by unpaired t test. Data are shown as mean \pm SD.

See also Figure S6 and Tables S3 and S4.

of crosslinking is substantially decreased at non-Uridine bases (Sugimoto et al., 2012), limiting the ability of IMPs to crosslink at a CA-rich motif. Thus, to complement our eCLIP profiling data, we performed RBNS to characterize the in vitro binding motif for full-length IMP1 and IMP2 proteins (each including all six RNA binding domains). This method revealed that recombinant IMP1 and IMP2 proteins harbor strong preferences for CA-rich motifs with a degenerate CAU within them, correlating well with the MAHWCA motifs identified for IMP2 and IMP3 using an independent in vitro method RNACompete (Ray et al., 2013) as well as the CA motif identified in DeepBind re-analysis of RNACompete data (Alipanahi et al., 2015). Profiling in vivo by

PAR-CLIP identified a similar but slightly altered motif (CAU) (Hafner et al., 2010), possibly influenced by crosslinking at 4SU nucleotides in PAR-CLIP. These motifs all share strong similarity with motifs described by detailed molecular studies of individual IMP targets (Chao et al., 2010). The CA-rich motif was significantly enriched in eCLIP peaks, providing further validation that this motif likely represents a major component of IMP1 and IMP2 binding. As IMP binding is often complex, requiring specific spacing of associated motifs to drive dimerization (potentially of multiple IMP family members) (Nielsen et al., 2004), more detailed biochemical studies should provide insight into whether the CA repeat is more critical for binding initiation or

stabilization of IMP complexes and what role these other motifs play in directing IMP target recognition.

Given the relatively small transcriptome change observed upon IMP1 knockdown in hESCs, we were surprised to observe that loss of IMP1 led to dramatic cellular phenotypes, including increased apoptosis and a loss of cell adhesion and cytoskeletal integrity. As IMP roles in maintenance of cell adhesion have been previously described (Gu et al., 2012; Vikesaa et al., 2006), we asked whether the cell adhesion defect in hESCs could be explained by known or novel targets. We observed that there was a specific enrichment for downregulation of integrin mRNAs, particularly those most strongly bound by IMP1 (Figure 5). Further analysis validated IMP regulation of the stability of *ITGB5*. These results indicate that in addition to known IMP1 regulatory targets such as *CTNNB1* and *CD44* that play critical roles in maintenance of proper cell adhesion (Gu et al., 2012; Vikesaa et al., 2006), the integrin family represents an additional cell adhesion regulatory mechanism for IMP1. Future work to determine whether integrin regulation by IMP1 is specific to hESCs or affects cell adhesion in other systems and the direct mechanisms (including additional co-factors) through which IMP1 binding modulates stability of *ITGB5* will provide further insight into the cell-type-specificity of the mechanisms through which IMPs regulate cell adhesion.

Although loss of cell adhesion partially explains the dramatic hESC cell viability defect upon IMP1 knockdown, we noted that apoptotic markers were also increased. Global analyses of either eCLIP-bound or differential transcripts did not show general enrichments for apoptosis or related pathways. However, closer inspection of IMP1 bound and responsive targets identified *BCL2*, which encodes a critical anti-apoptotic protein, as another IMP1 target that decreases upon IMP1 depletion in hPSCs. Pursuing this further due to the well-characterized roles of *BCL2* in mediating apoptotic signals, we found that re-expression of *BCL2* in hESCs partially rescued the cell death phenotype resulting from IMP1 depletion in a dose-dependent manner, confirming the contribution of *BCL2* to IMP1 knockdown phenotypes in hESCs. The linkage of IMP1 with direct regulation of *BCL2* further associates IMP1 with known oncogenic pathways and may provide an interesting avenue for further studies of IMP1 in other cell types, particularly with respect to understanding its roles in modulating tumorigenesis and metastasis. Thus, our results indicate that we are far from an exhaustive list of functional IMP family targets, and further elucidation of the direct and regulated targets of IMP proteins in their various cellular contexts (whether in normal or cancerous cell-types) may provide insights into the distinct and shared roles these proteins play in development and tumorigenesis.

EXPERIMENTAL PROCEDURES

eCLIP-Seq Experimental Procedures

UV-crosslinked (10×10^6) (400 mJ/cm² constant energy) H9ES (IMPs, IgG) or H1ES (RBFOX2) cells were lysed in iCLIP lysis buffer and sonicated (BioRuptor). Lysate was treated with RNase I (Ambion) to fragment RNA, after which IMP1 (MBL, #RN007P), IMP2 (MBL, #RN008P), IMP3 (MBL, #RN009P), RBFOX2 (Bethyl Laboratories, #A300-864A), and rabbit IgG (Life Technologies) protein-RNA complexes were immunoprecipitated using the indicated antibody. In addition to the RBP-IPs a parallel size-matched input (SMinput) library was

generated; these samples were not immunoprecipitated with anti-RBP antibodies but were otherwise treated identically (to aid in the removal of false positives). One SMinput was used for each biological replicate grouping of all IMP proteins due to their similarity in molecular weight, with a separate SMinput generated for RBFOX2. Stringent washes were performed as described in iCLIP, during which RNA was dephosphorylated with FastAP (Fermentas) and T4 PNK (NEB). Subsequently, a 3' RNA adaptor was ligated onto the RNA with T4 RNA ligase (NEB). Protein-RNA complexes were run on an SDS-PAGE gel, transferred to nitrocellulose membranes, and RNA was isolated off the membrane identically to standard iCLIP. After precipitation, RNA was reverse transcribed with AffinityScript (Agilent), free primer was removed (ExoSap-IT, Affymetrix), and a 3' DNA adaptor was ligated onto the cDNA product with T4 RNA ligase (NEB). Libraries were then amplified with Q5 PCR mix (NEB). See Van Nostrand et al. (2016) for further details regarding standardized eCLIP experimental workflows.

eCLIP-Seq Read Processing and Cluster Analysis

Briefly, reads were adaptor trimmed (cutadapt), mapped against repetitive elements (with repeat-mapping reads discarded), and then mapped to the human genome with STAR. PCR duplicate reads were removed, and the second (paired-end) read was used to perform peak-calling with CLIPper (Lovci et al., 2013). Region-level analysis was performed by counting reads overlapping regions annotated in Gencode (v19). Input normalization of peaks was performed by counting reads mapping to CLIPper-identified peaks in eCLIP and paired SMinput datasets, with significance thresholds of $p \leq 10^{-5}$ and fold enrichment ≥ 8 . See the *Supplemental Experimental Procedures* for further details and Van Nostrand et al. (2016) for software packages used and additional description of processing steps.

hPSC Cell Culture

All hPSC lines (including H9, H1, HUES6, and iPSC) lines were grown on Matrigel (BD Biosciences) using mTeSR1 medium (Stem Cell Technologies). Cells were routinely passaged using Dispase (2 mg/ml) and scraping the colonies with a glass pipet. For assays requiring single-cell dissociation, Accutase (Innovative Cell Technologies) was used followed by culture medium supplemented with 10 μM Rock Inhibitor Y-27632 (Calbiochem) for 24 hr. See the *Supplemental Experimental Procedures* for further details.

Lentiviral Vectors, Production, and hESC Infection

If not otherwise indicated, experiments were performed using pLKO lentivirus constructs TRCN0000075149 for IMP1, TRCN0000255463 for IMP2, TRCN0000074675 for IMP3, and non-target control Sigma #SHC002 (that targets turboGFP). Two additional shRNAs were tested for IMP1, TRCN0000218079 that targeted the CDS (shRNA 2) and TRCN0000230114 that targets the IMP1 3' UTR (shRNA 3). Unless otherwise noted, shRNA 3 (TRCN0000230114) was used as the second shRNA for phenotypic experiments. See the *Supplemental Experimental Procedures* for additional details.

Adhesion Assay

After virus transduction and puromycin selection, hES cells were plated out at 50,000 cells per well in a 96-well plate coated with Matrigel, incubated for 1 hr at 37°C with 5% CO₂, vortexed at 2,000 rpm for 15 s, washed three times with 0.1% BSA in DMEM/F12, and fixed with 4% paraformaldehyde for 10 min at room temperature. Following fixation, cells were washed with 0.1% BSA in DMEM/F12 and stained with crystal violet (5 mg/ml in 2% EtOH) for 10 min. Cells were then rinsed with H₂O and left to completely dry for 15 min. SDS (2%) was added for 20 min followed by absorbance reading on a plate reader. Data are represented as mean ± SD, with statistical significance calculated by unpaired t test.

BCL2 Rescue Apoptosis Assay

H9 hESCs expressing control and IMP1 shRNAs were split into four biological replicates each and transduced with dox-inducible BCL2 viruses. After 24 hr, three replicates were each re-plated into four wells of a 96-well plate at a density of 20,000 cells per well. A titration of doxycycline was added for 24 hr after which apoptosis was measured by the Caspase-Glo 3/7 assay (Promega). The Caspase-Glo 3/7 assay was performed according to the

manufacturer's instructions. The fourth replicate was collected in parallel for western blot analysis of BCL2 induction. Luminescence and fluorescence data were averaged across the four technical replicate wells and are represented as mean \pm SD of biological replicates, with statistical significance calculated by unpaired t test.

Western Blot

Cells were washed with PBS and lysed with lysis buffer (10 mM Tris-HCl [pH 8], 150 mM NaCl, 1% Triton X-100 and complete protease inhibitor mixture [Roche]). Total protein extracts were run on 4%–12% NuPAGE Bis-Tris gels in NuPAGE MOPS running buffer (Thermo Fisher), transferred to nitrocellulose membranes (Amersham Biosciences) and analyzed using primary antibodies. Primary antibodies were incubated overnight at 4°C and secondary HRP conjugated antibodies (Jackson ImmunoResearch, 1:10,000) were incubated for 1 hr at room temperature. Thermo Pierce ECL detection reagents were used. See the [Supplemental Experimental Procedures](#) for full list of antibodies used.

RNA Extraction and qRT-PCR Analysis

Total RNA was isolated using Trizol Reagent (Invitrogen) according to the manufacturer's recommendations, DNase treated with Turbo DNA-free kit (Ambion), and cDNA synthesized from 2 μ g total RNA using the SuperScript III Reverse Transcriptase kit for qRT-PCR (Invitrogen). Both random hexamers and oligo(dT) primers were used for reverse transcription. Real-time PCR was performed using the SYBR-Green FAST qPCR Master mix (Applied Biosystems) on a CFX384 Touch Real-Time PCR Detection System (Bio-Rad). Values of gene expression were normalized using an average of 18s, GAPDH, and HMBS with the exception of the Actinomycin D experiments (see [Figure 5K](#) and [Experimental Procedures](#) for details) and are shown as fold change relative to the value of the control shRNA-treated sample. All experiments were performed in technical and biological triplicates. Bars indicate mean \pm SEM as measured by the $\Delta\Delta Ct$ method. Significance was determined by unpaired t test between the control shRNA sample and IMP1 shRNA sample. See the [Supplemental Experimental Procedures](#) for primer sequences used.

Actinomycin D RNA Stability Assay

H9 hESCs were treated with 10 μ g/ml actinomycin D (Sigma) and RNA was isolated using Trizol at time 0 (no treatment), 60 min, and 120 min after treatment. RNA decay was measured with qRT-PCR normalized to the amount of RNA at time 0 (see [RNA Extraction and qRT-PCR Analysis](#)). Values of gene expression were normalized using *PP1A* and *RPLP0*, genes determined not to change over the given time period following addition of actinomycin D.

RNA Immunoprecipitation Assay in hESCs

RNA immunoprecipitation (RIP) was performed with an input of $\sim 20 \times 10^6$ uncrosslinked HUES6 hES cells lysed with CLIP lysis buffer ([Wilbert et al., 2012](#)). A total of 5 μ g of each antibody, Rabbit IgG (Santa Cruz, #SC-2027) and IMP1 (MBL, #RN007P), were coupled to Protein G Dynabeads (Invitrogen) and incubated with pre-cleared cell lysate overnight on rotation at 4°C. Immunoprecipitated RNA was isolated from beads using 1 ml Trizol according to the manufacturer's instructions and reverse-transcribed using the SuperScript III Reverse Transcriptase kit. Endpoint RT-PCR was performed using Crimson Taq DNA Polymerase (NEB).

Electrophoretic Mobility Shift Assay

IMP1 electrophoretic mobility shift assay (EMSA) was performed based on the conditions used in [Farina et al. \(2003\)](#). Binding reactions contained the following: 10 mM Tris [pH 7.5], 50 mM NaCl, 1 mM MgCl₂, 0.5 mM EDTA, 0.5 mM DTT, 4% glycerol, 100 ng *Escherichia coli* tRNA (Roche), 10,000 cpm of the ³²P-labeled target RNA, and increasing amounts of recombinant human IMP1 protein (Origene #TP316226) to a final volume of 20 μ l. Reactions were incubated for 30 min at room temperature followed by 15 min on ice. Reactions were loaded on 5% nondenaturing polyacrylamide TGE gels containing 5% glycerol and run at 150 V for 2 hr. Following electrophoresis, gels were dried and exposed to phosphoimager film. See the [Supplemental Experimental Procedures](#) for further details.

RNA Bind-N-Seq

RNA Bind-N-seq (RBNS) was performed on full-length GST-SBP-tagged IMP1 and IMP2 as previously described ([Lambert et al., 2014](#)). The motif frequency in the RBP-selected pool divided by the frequency in the input RNA library was calculated for all *k*-mers (*k* = 4, 5, 6) and defined as the motif enrichment (R) value. Mean and SD of R values were calculated across all *k*-mers for each *k* (4-mers, 5-mers, and 6-mers), with significance thresholds set at *Z* score \geq 2. Enrichments from the protein concentration with the greatest enrichment were used for comparison with CLIP peaks, compared against same-sized regions randomly selected from the same genomic region (e.g., 3' UTRs or CDS). See the [Supplemental Experimental Procedures](#) for additional details.

ACCESSION NUMBERS

The accession number for the IMP eCLIP and knockdown RNA-seq data reported in this paper is GEO: GSE78509. The accession numbers for the Bind-N-Seq datasets reported in this paper are ENCODE DCC (<https://www.encodeproject.org>): ENCSR928XOW (IMP1) and ENCSR588GYZ (IMP2).

SUPPLEMENTAL INFORMATION

Supplemental Information includes Supplemental Experimental Procedures, six figures, and four tables and can be found with this article online at <http://dx.doi.org/10.1016/j.celrep.2016.03.052>.

AUTHOR CONTRIBUTIONS

Conceptualization, A.E.C., E.L.V.N., M.L.W., D.L.J., and G.W.Y.; Investigation, A.E.C., E.L.V.N., S.A., B.S., M.L.W., T.Y.L., P.F., and N.J.L.; Validation, A.E. and S.L.; Formal Analysis, A.E.C., E.L.V.N., G.A.P., and S.S.; Writing – Original Draft, A.E.C., E.L.V.N., M.L.W., D.L.J., and G.W.Y.; Writing – Review & Editing, A.E.C., E.L.V.N., D.L.J., and G.W.Y.; Funding Acquisition, C.B.B., D.L.J., and G.W.Y.; Supervision, D.L.J. and G.W.Y.

ACKNOWLEDGMENTS

We thank members of the D.L.J. and G.W.Y. labs for constructive discussions and comments on the manuscript and the Salk Institute Stem Cell Core, especially Dr. Travis Berggren, Margaret Lutz, and Ken Diffenderfer for their invaluable assistance. We thank Patrick Liu for computational analysis assistance and Reza Ardehali, Matt Inlay, and Irving Weissman for sharing BCL2 plasmids. This work was supported by the Eli and Edythe Broad Center of Regenerative Medicine and Stem Cell Research at the University of California, Los Angeles, and a California Institute of Regenerative Medicine (CIRM) New Faculty Award (RN1-00544) to D.L.J. and by grants from the NIH (HG004659, NS075449, and U54HG007005) and CIRM (RB1-01413 and RB3-05009) to G.W.Y., and was partially supported by NIH grant HG007005 to C.B.B. A.E.C. and M.L.W. were supported in part by the University of California, San Diego, Genetics Training Program through an institutional training grant from the NIGMS, T32 GM008666. S.L. and A.E. were supported by Pioneer postdoctoral fellowship awards from the Salk Institute for Biological Studies. M.L.W. was a CIRM pre-doctoral fellow. E.L.V.N. is a Merck Fellow of the Damon Runyon Cancer Research Foundation (DRG-2172-13), and G.W.Y. was an Alfred P. Sloan Research Fellow.

Received: December 24, 2015

Revised: February 17, 2016

Accepted: March 11, 2016

Published: April 7, 2016

REFERENCES

- Alipanahi, B., Delong, A., Weirauch, M.T., and Frey, B.J. (2015). Predicting the sequence specificities of DNA- and RNA-binding proteins by deep learning. *Nat. Biotechnol.* 33, 831–838.

- Ardehali, R., Inlay, M.A., Ali, S.R., Tang, C., Drukker, M., and Weissman, I.L. (2011). Overexpression of BCL2 enhances survival of human embryonic stem cells during stress and obviates the requirement for serum factors. *Proc. Natl. Acad. Sci. USA* 108, 3282–3287.
- Atlas, R., Behar, L., Sapoznik, S., and Ginzburg, I. (2007). Dynamic association with polysomes during P19 neuronal differentiation and an untranslated-region-dependent translation regulation of the tau mRNA by the tau mRNA-associated proteins IMP1, HUD, and G3BP1. *J. Neurosci. Res.* 85, 173–183.
- Bell, J.L., Wächter, K., Mühlbeck, B., Pazaitis, N., Köhn, M., Lederer, M., and Hüttelmaier, S. (2013). Insulin-like growth factor 2 mRNA-binding proteins (IGF2BPs): post-transcriptional drivers of cancer progression? *Cell. Mol. Life Sci.* 70, 2657–2675.
- Bernstein, P.L., Herrick, D.J., Prokipcak, R.D., and Ross, J. (1992). Control of c-myc mRNA half-life in vitro by a protein capable of binding to a coding region stability determinant. *Genes Dev.* 6, 642–654.
- Braam, S.R., Zeinstra, L., Litjens, S., Ward-van Oostwaard, D., van den Brink, S., van Laake, L., Lebrin, F., Kats, P., Hochstenbach, R., Passier, R., et al. (2008). Recombinant vitronectin is a functionally defined substrate that supports human embryonic stem cell self-renewal via alphavbeta5 integrin. *Stem Cells* 26, 2257–2265.
- Chao, J.A., Patskovsky, Y., Patel, V., Levy, M., Almo, S.C., and Singer, R.H. (2010). ZBP1 recognition of beta-actin zipcode induces RNA looping. *Genes Dev.* 24, 148–158.
- Dai, N., Rapley, J., Angel, M., Yanik, M.F., Blower, M.D., and Avruch, J. (2011). mTOR phosphorylates IMP2 to promote IGF2 mRNA translation by internal ribosomal entry. *Genes Dev.* 25, 1159–1172.
- Dai, N., Christiansen, J., Nielsen, F.C., and Avruch, J. (2013). mTOR complex 2 phosphorylates IMP1 cotranslationally to promote IGF2 production and the proliferation of mouse embryonic fibroblasts. *Genes Dev.* 27, 301–312.
- Dai, N., Zhao, L., Wrighting, D., Krämer, D., Majithia, A., Wang, Y., Cracan, V., Borges-Rivera, D., Mootha, V.K., Nahrendorf, M., et al. (2015). IGF2BP2/IMP2-Deficient mice resist obesity through enhanced translation of Ucp1 mRNA and Other mRNAs encoding mitochondrial proteins. *Cell Metab.* 21, 609–621.
- Dimitriadis, E., Trangas, T., Milatos, S., Foukas, P.G., Gioulbasanis, I., Courtis, N., Nielsen, F.C., Pandis, N., Dafni, U., Bardi, G., and Ioannidis, P. (2007). Expression of oncofetal RNA-binding protein CRD-BP/IMP1 predicts clinical outcome in colon cancer. *Int. J. Cancer* 121, 486–494.
- Farina, K.L., Huttelmaier, S., Musunuru, K., Darnell, R., and Singer, R.H. (2003). Two ZBP1 KH domains facilitate beta-actin mRNA localization, granule formation, and cytoskeletal attachment. *J. Cell Biol.* 160, 77–87.
- Gu, W., Wells, A.L., Pan, F., and Singer, R.H. (2008). Feedback regulation between zipcode binding protein 1 and beta-catenin mRNAs in breast cancer cells. *Mol. Cell. Biol.* 28, 4963–4974.
- Gu, W., Katz, Z., Wu, B., Park, H.Y., Li, D., Lin, S., Wells, A.L., and Singer, R.H. (2012). Regulation of local expression of cell adhesion and motility-related mRNAs in breast cancer cells by IMP1/ZBP1. *J. Cell Sci.* 125, 81–91.
- Hafner, M., Landthaler, M., Burger, L., Khoshid, M., Hausser, J., Berninger, P., Rothballer, A., Ascano, M., Jr., Jungkamp, A.C., Munschauer, M., et al. (2010). Transcriptome-wide identification of RNA-binding protein and microRNA target sites by PAR-CLIP. *Cell* 141, 129–141.
- Hammer, N.A., Hansen, T.V.O., Byskov, A.G., Rajpert-De Meyts, E., Grøndahl, M.L., Bredkjaer, H.E., Wewer, U.M., Christiansen, J., and Nielsen, F.C. (2005). Expression of IGF-II mRNA-binding proteins (IMPs) in gonads and testicular cancer. *Reproduction* 130, 203–212.
- Han, H., Irimia, M., Ross, P.J., Sung, H.K., Alipanahi, B., David, L., Golipour, A., Gabut, M., Michael, I.P., Nachman, E.N., et al. (2013). MBNL proteins repress ES-cell-specific alternative splicing and reprogramming. *Nature* 498, 241–245.
- Hansen, T.V.O., Hammer, N.A., Nielsen, J., Madsen, M., Dalbaeck, C., Wewer, U.M., Christiansen, J., and Nielsen, F.C. (2004). Dwarfism and impaired gut development in insulin-like growth factor II mRNA-binding protein 1-deficient mice. *Mol. Cell. Biol.* 24, 4448–4464.
- Hüttelmaier, S., Zenklusen, D., Lederer, M., Dictenberg, J., Lorenz, M., Meng, X., Bassell, G.J., Condeelis, J., and Singer, R.H. (2005). Spatial regulation of beta-actin translation by Src-dependent phosphorylation of ZBP1. *Nature* 438, 512–515.
- Janiszewska, M., Suvà, M.L., Riggi, N., Houtkooper, R.H., Auwerx, J., Clément-Schatlo, V., Radovanovic, I., Rheinbay, E., Provero, P., and Stamenkovic, I. (2012). Imp2 controls oxidative phosphorylation and is crucial for preserving glioblastoma cancer stem cells. *Genes Dev.* 26, 1926–1944.
- Jønson, L., Vikesaa, J., Krogh, A., Nielsen, L.K., Hansen, T.V., Borup, R., Johnsen, A.H., Christiansen, J., and Nielsen, F.C. (2007). Molecular composition of IMP1 ribonucleoprotein granules. *Mol. Cell. Proteomics* 6, 798–811.
- Konig, J., Zarnack, K., Rot, G., Curk, T., Kayikci, M., Zupan, B., Turner, D.J., Luscombe, N.M., and Ule, J. (2011). iCLIP—transcriptome-wide mapping of protein-RNA interactions with individual nucleotide resolution. *J. Vis. Exp.* (50), 2638.
- Lambert, N., Robertson, A., Jangi, M., McGahey, S., Sharp, P.A., and Burge, C.B. (2014). RNA Bind-n-Seq: quantitative assessment of the sequence and structural binding specificity of RNA binding proteins. *Mol. Cell* 54, 887–900.
- Lee, S.R., Pratt, G.A., Martinez, F.J., Yeo, G.W., and Lykke-Andersen, J. (2015). Target discrimination in nonsense-mediated mRNA decay requires Upf1 ATPase activity. *Mol. Cell* 59, 413–425.
- Leeds, P., Kren, B.T., Boylan, J.M., Betz, N.A., Steer, C.J., Gruppuso, P.A., and Ross, J. (1997). Developmental regulation of CRD-BP, an RNA-binding protein that stabilizes c-myc mRNA in vitro. *Oncogene* 14, 1279–1286.
- Li, Q., Brown, J.B., Huang, H., and Bickel, P.J. (2011). Measuring reproducibility of high-throughput experiments. *Ann. Appl. Stat.* 5, 1752–1779.
- Lovci, M.T., Ghanem, D., Marr, H., Arnold, J., Gee, S., Parra, M., Liang, T.Y., Stark, T.J., Gehman, L.T., Hoon, S., et al. (2013). Rbf1 proteins regulate alternative mRNA splicing through evolutionarily conserved RNA bridges. *Nat. Struct. Mol. Biol.* 20, 1434–1442.
- Marchetto, M.C., Narvaiza, I., Denli, A.M., Benner, C., Lazzarini, T.A., Nathanson, J.L., Paquola, A.C., Desai, K.N., Herai, R.H., Weitzman, M.D., et al. (2013). Differential L1 regulation in pluripotent stem cells of humans and apes. *Nature* 503, 525–529.
- Nielsen, J., Christiansen, J., Lykke-Andersen, J., Johnsen, A.H., Wewer, U.M., and Nielsen, F.C. (1999). A family of insulin-like growth factor II mRNA-binding proteins represses translation in late development. *Mol. Cell. Biol.* 19, 1262–1270.
- Nielsen, F.C., Nielsen, J., Kristensen, M.A., Koch, G., and Christiansen, J. (2002). Cytoplasmic trafficking of IGF-II mRNA-binding protein by conserved KH domains. *J. Cell Sci.* 115, 2087–2097.
- Nielsen, J., Kristensen, M.A., Willemoes, M., Nielsen, F.C., and Christiansen, J. (2004). Sequential dimerization of human zipcode-binding protein IMP1 on RNA: a cooperative mechanism providing RNP stability. *Nucleic Acids Res.* 32, 4368–4376.
- Ray, D., Kazan, H., Cook, K.B., Weirauch, M.T., Najafabadi, H.S., Li, X., Gueroussov, S., Albu, M., Zheng, H., Yang, A., et al. (2013). A compendium of RNA-binding motifs for decoding gene regulation. *Nature* 499, 172–177.
- Ross, A.F., Oleynikov, Y., Kislauskis, E.H., Taneja, K.L., and Singer, R.H. (1997). Characterization of a beta-actin mRNA zipcode-binding protein. *Mol. Cell. Biol.* 17, 2158–2165.
- Ross, J., Lemm, I., and Berberet, B. (2001). Overexpression of an mRNA-binding protein in human colorectal cancer. *Oncogene* 20, 6544–6550.
- Sugimoto, Y., König, J., Hussain, S., Zupan, B., Curk, T., Frye, M., and Ule, J. (2012). Analysis of CLIP and iCLIP methods for nucleotide-resolution studies of protein-RNA interactions. *Genome Biol.* 13, R67.
- Van Nostrand, E.L., Pratt, G.A., Shishkin, A.A., Gelboin-Burkhart, C., Fang, M.Y., Sundaraman, B., Blue, S.M., Nguyen, T.B., Surka, C., Elkins, K., et al. (2016). Robust transcriptome-wide discovery of RNA binding protein binding sites with enhanced CLIP (eCLIP). *Nat. Methods*, Published online March 28, 2016. <http://dx.doi.org/10.1038/nmeth.3810>.

- Vikesaa, J., Hansen, T.V., Jønson, L., Borup, R., Wewer, U.M., Christiansen, J., and Nielsen, F.C. (2006). RNA-binding IMPs promote cell adhesion and invadopodia formation. *EMBO J.* 25, 1456–1468.
- Wagenmakers, A.J., Reinders, R.J., and van Venrooij, W.J. (1980). Cross-linking of mRNA to proteins by irradiation of intact cells with ultraviolet light. *Eur. J. Biochem.* 112, 323–330.
- Wilbert, M.L., Huelga, S.C., Kapeli, K., Stark, T.J., Liang, T.Y., Chen, S.X., Yan, B.Y., Nathanson, J.L., Hutt, K.R., Lovci, M.T., et al. (2012). LIN28 binds messenger RNAs at GGAGA motifs and regulates splicing factor abundance. *Mol. Cell* 48, 195–206.
- Wu, B., Buxbaum, A.R., Katz, Z.B., Yoon, Y.J., and Singer, R.H. (2015). Quantifying protein-mRNA interactions in single live cells. *Cell* 162, 211–220.
- Yeo, G.W., Coufal, N.G., Liang, T.Y., Peng, G.E., Fu, X.D., and Gage, F.H. (2009). An RNA code for the FOX2 splicing regulator revealed by mapping RNA-protein interactions in stem cells. *Nat. Struct. Mol. Biol.* 16, 130–137.

Supplemental Information

**Enhanced CLIP Uncovers IMP Protein-RNA Targets
in Human Pluripotent Stem Cells Important
for Cell Adhesion and Survival**

Anne E. Conway, Eric L. Van Nostrand, Gabriel A. Pratt, Stefan Aigner, Melissa L. Wilbert, Balaji Sundararaman, Peter Freese, Nicole J. Lambert, Shashank Sathe, Tiffany Y. Liang, Anthony Essex, Severine Landais, Christopher B. Burge, D. Leanne Jones, and Gene W. Yeo

Inventory of Supplemental Information:

Figures and Tables:

Figure S1: Related to Figure 2, IMP RBPs bind thousands of target RNAs in hESCs.

Figure S2: Related to Figure 2, IMP1 and IMP2 show highly correlated binding to 3'UTR regions.

Figure S3: Related to Figure 3, IMP1 and IMP2 show correlated, reproducible binding peaks.

Figure S4: Related to Figure 4, IMP1 and IMP2 *in vitro* binding motifs identified by RNA Bind-N-Seq (RBNS).

Figure S5: Related to Figure 5, IMP1 binds target genes important for regulating cytoskeletal architecture in hESC.

Figure S6: Related to Figure 6, IMP1 has little effect on cell proliferation but promotes cell survival through regulation of BCL2 in hESCs.

Table S1: Related to Figure 2, eCLIP sequencing library processing summary metrics.

Table S2: Related to Figures 2 and 3, eCLIP fold-enrichment values across genic regions (attached as an individual excel file).

Table S3: Related to Figures 5 and 6, RNA-seq processing summary metrics.

Table S4: Related to Figures 5 and 6, RNA-seq differential expression analysis of Control KD versus IMP1 knockdown hESCs (attached as an individual excel file).

Supplemental Experimental Procedures.

Figure S1.

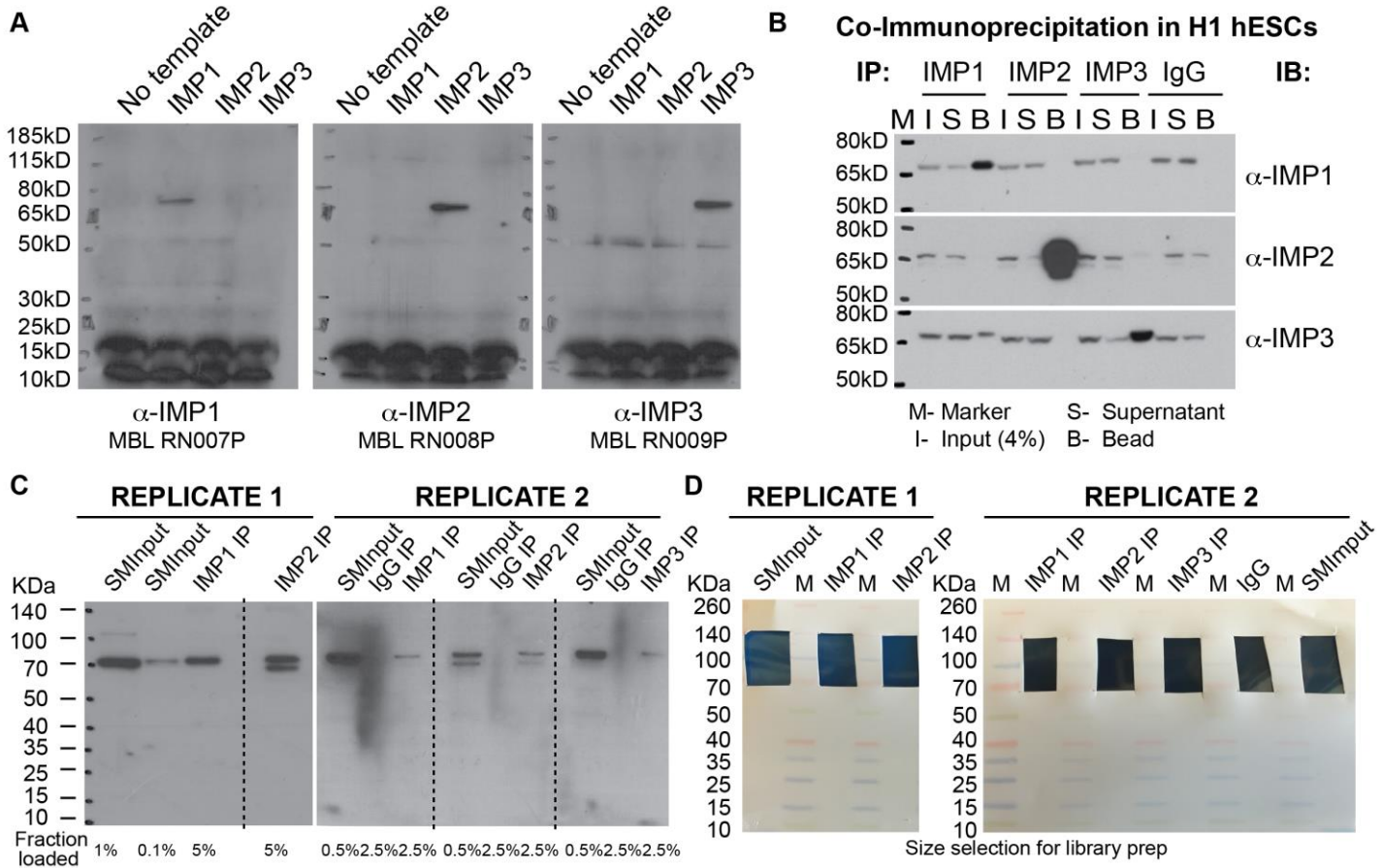


Figure S1: Related to Figure 2, IMP RBPs bind thousands of target RNAs in hESCs.

(A) Recombinant human IMP protein expression in rabbit reticulolysates followed by Western blot for IMP1, IMP2, and IMP3. (B) Western blot of immunoprecipitation of IMP1, IMP2, and IMP3 in H1 hESC, showing co-immunoprecipitation of other family members. (C) Western blot validation of immunoprecipitation performed during eCLIP of IMP1, IMP2, and IMP3. (D) Images show nitrocellulose membranes cut during eCLIP of IMP1, IMP2, and IMP3, indicating the size range from which RNA was isolated.

Figure S2.

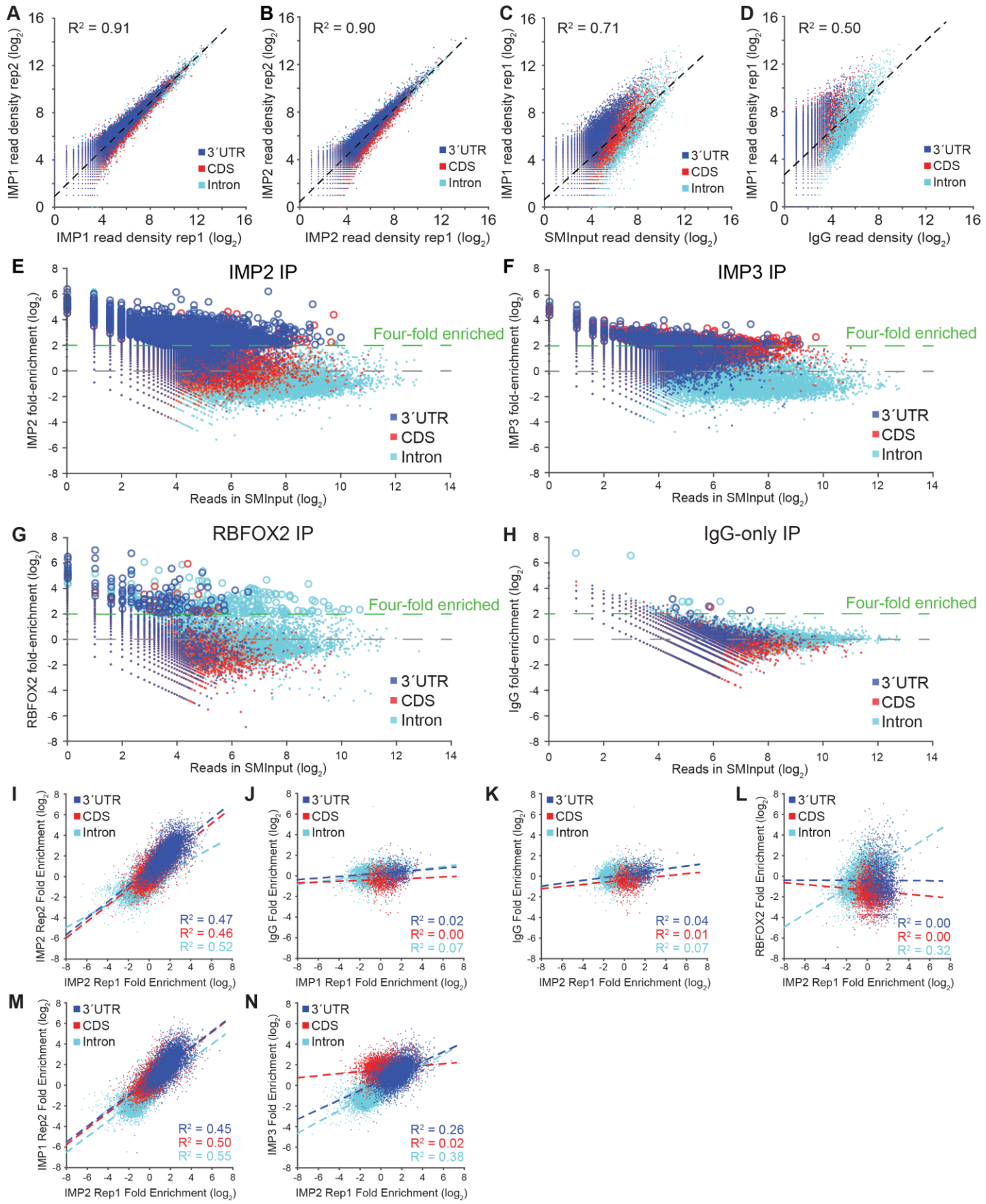


Figure S2: Related to Figure 2, IMP1 and IMP2 show highly correlated binding to 3'UTR regions.

(A-D) eCLIP read density comparison across replicates and samples, with black dotted line and correlation reflecting least-squares regression line through all points. (A) Read density observed in two biological replicates of IMP1 eCLIP for 3'UTRs (navy), coding sequence exons (red), and introns (cyan). (B) Region-based read density observed for IMP2 biological replicate eCLIP experiments. (C) Region-based read density observed between IMP1 Rep1 (y-axis) and paired SMInput (x-axis) eCLIP. IMP1 Rep2 and IMP2 (Rep1 and Rep2) showed similar results (data not shown). (D) Region-based read density observed between IMP1 Rep1 (y-axis) and IgG (x-axis) eCLIP. IgG overlap with IMP2 Rep1 showed similar results (data not shown). (E-H) Region-based fold-enrichment in eCLIP over paired SMInput. eCLIP read density relative to paired SMInput experiments is shown for (E) IMP2 biological replicate 2, (F) IMP3, (G) RBFOX2, and (H) IgG. As in Figure 2B, read density was counted separately for 3'UTR (blue), CDS (red), or introns (cyan). Scatter plot indicates fold-enrichment for each region in eCLIP relative to paired SMInput (y-axis), plotted against read density in SMInput (x-axis). Green dotted line indicates four-fold enrichment cutoff, and open circles indicate regions significantly enriched in eCLIP relative to SMInput ($p \leq 10^{-5}$ and ≥ 4 -fold). (I) eCLIP fold-enrichment comparison across replicates and samples. Fold-enrichment of IMP2 biological replicate 1 over paired SMInput (x-axis) versus IMP2 biological replicate 2 over paired SMInput (y-axis). Dotted lines and R^2 values indicate least squares regression performed separately for each region type. (J-N) Similar plots reflecting (J) IMP1 versus IgG region-based fold-enrichment, (K) IMP2 versus IgG region-based fold-enrichment, (L) IMP2 versus RBFOX2 region-based fold-enrichment, (M) IMP2 Rep1 versus IMP1 Rep2 region-based fold-enrichment and (N) IMP2 versus IMP3 region-based fold-enrichment.

Figure S3.

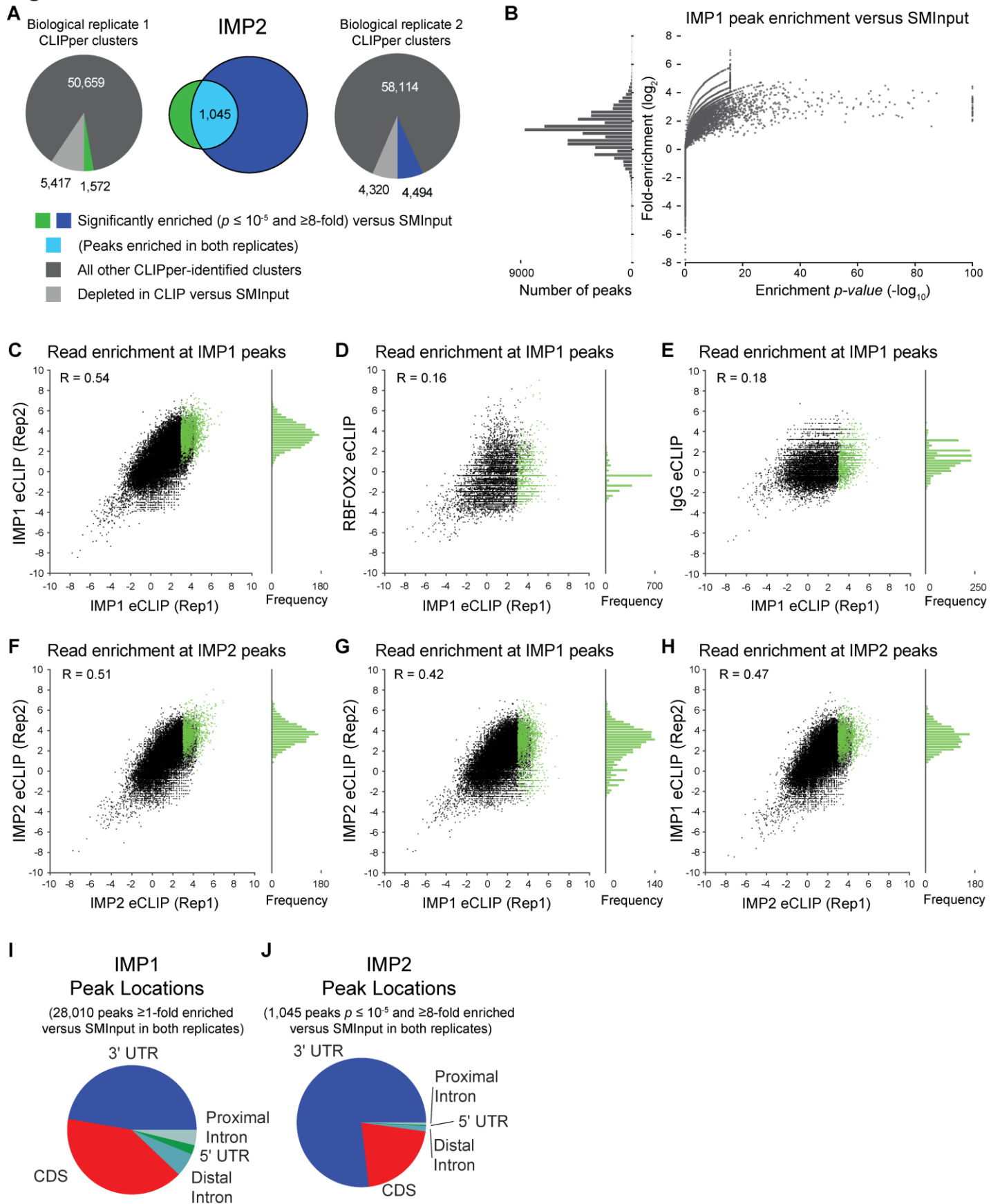
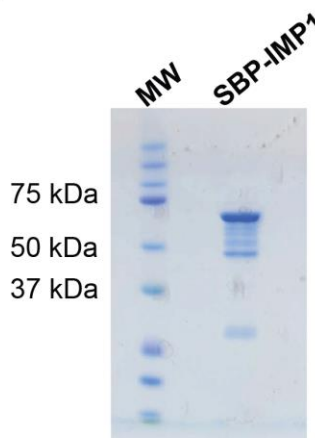


Figure S3. Related to Figure 3, IMP1 and IMP2 show correlated, reproducible binding peaks.

(A) IMP2 clusters are shown as in Figure 3A; pie charts indicate the fraction of CLIPper-identified clusters (grey) that show enriched read coverage in CLIP above SMInput (green & blue), with overlap across biological replicates indicated in light blue (center). (B) Scatter plot indicates the enrichment p -value (by Yates' Chi-Square test, or Fisher's Exact Test if read number was below 5 (see Methods)) and fold-enrichment between IP and SMInput for IMP1 (Rep1) CLIPper-identified cluster regions. The distribution of clusters by fold-enrichment is indicated by the left histogram. (C-H) For clusters identified in one eCLIP dataset (x-axis), scatter plots indicate the IP-to-SMInput enrichment for this set of regions across two datasets. The subset of IP-enriched ($p \leq 10^{-5}$, ≥ 8 -fold enriched versus SMInput) peaks are indicated in green, with attached histogram indicating distribution along the second dataset (y-axis). Correlation indicated is from comparison of all clusters (black + green). Figures compare (C) IMP1 biological replicates, (D) IMP1 versus RBFOX2, (E) IMP1 versus IgG, (F) IMP2 biological replicates, (G) IMP1 versus IMP2, and (H) IMP2 versus IMP1. (I-J) Pie charts indicate the distribution of (I) IMP1 CLIP-enriched or (J) IMP2 significantly enriched peaks overlapping genic coding sequence (CDS), 3' or 5' untranslated regions, and distal (more than 500nt from the splice site) and proximal (within 500nt of the splice site) intronic regions.

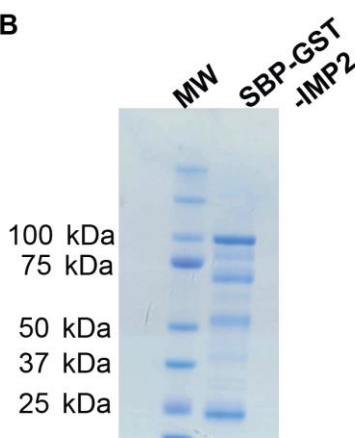
Figure S4.

A



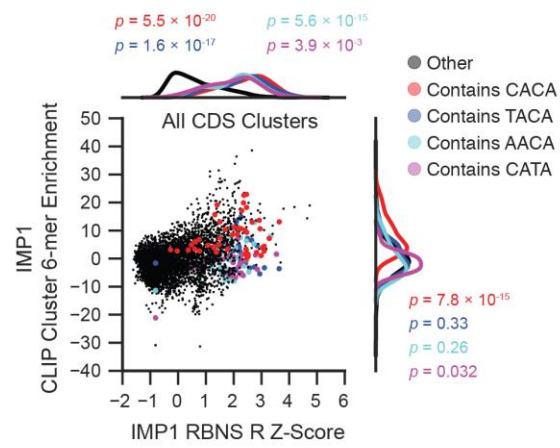
Expected size: 63kDa

B



Expected size: 95kDa

C



D

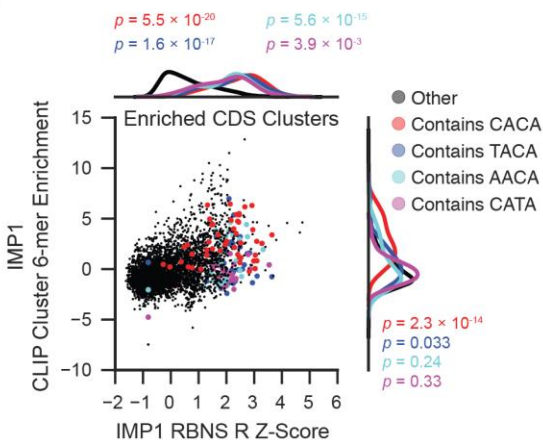


Figure S4: Related to Figure 4, IMP1 and IMP2 *in vitro* binding motifs identified by RNA Bind-N-Seq (RBNS).

(A-B) Coomassie staining of recombinantly expressed and GST purified full-length IMP1 and IMP2 protein size-separated by gel electrophoresis. (C-D) Comparison between motif enrichments identified in eCLIP and RBNS of IMP1. IMP1 RBNS motif enrichment (x-axis) plotted against IMP1 eCLIP motif enrichment (y-axis) for all 6-mers (black dots) or 6-mers containing a CACA 4-mer (red), TACA (navy), AACCA (light blue), or CATA (magenta). Kernel-smoothed density plots for all motifs (black line) and 4-mer-containing motifs (colored lines) are shown for RBNS (top) and eCLIP (right), with significance determined by Kolmogorov-Smirnov test. Panels show motif analysis for (C) all IMP1 CDS clusters or (D) stringent IMP1 CDS peaks (defined as $p \leq 10^{-5}$ and ≥ 8 -fold enrichment above SMInput).

Figure S5.

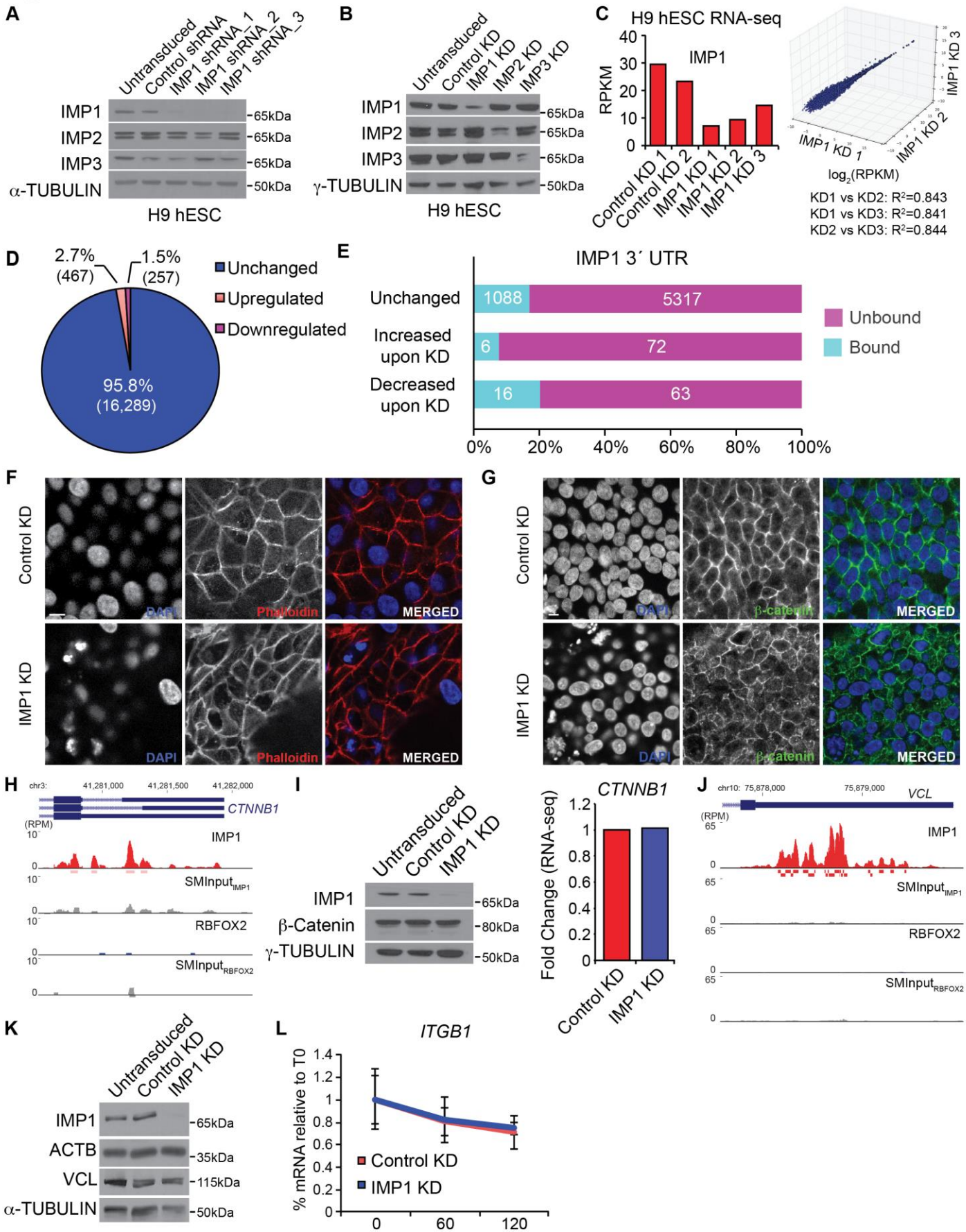
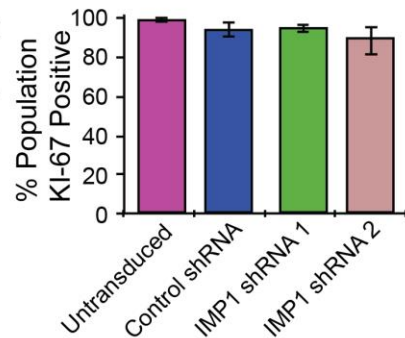
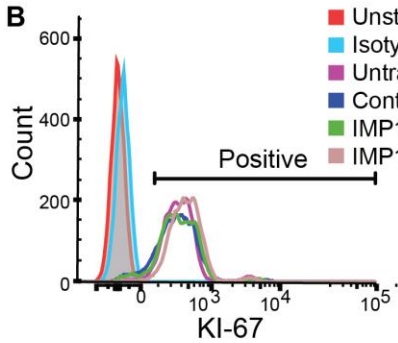
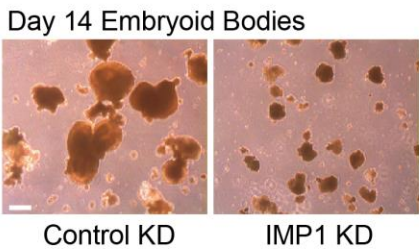


Figure S5: Related to Figure 5, IMP1 binds target genes important for regulating cytoskeletal architecture in hESC.

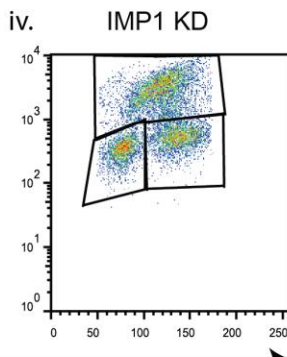
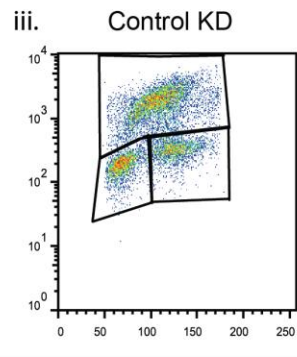
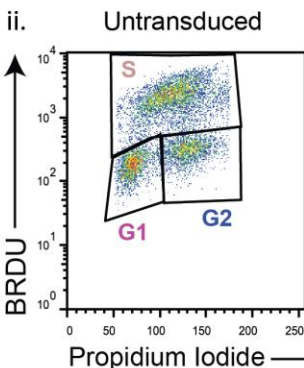
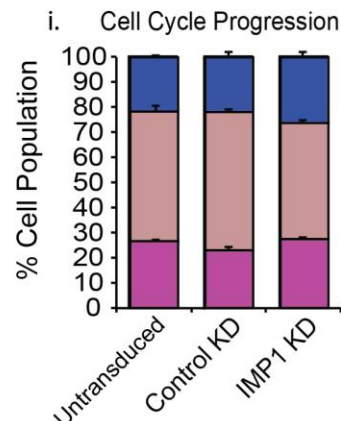
(A) Western blot displaying IMP1, IMP2 and IMP3 protein expression following depletion of IMP1 using three different shRNAs in H9 hESCs (#1-TRCN0000075149, #2-TRCN0000218079 and #3-TRCN0000230114). (B) Western blot displaying specificity of shRNAs targeting each of the three IMP family members, IMP1, IMP2, and IMP3. (C) (left) Bars indicate IMP1 reads per million mapped reads (RPKM) in samples used for RNA-seq. (right) Points indicate RPKM (\log_2) for all genes quantified by RNA-seq. See Table S3 for overall RNA-seq processing statistics, and Table S4 for differential gene expression quantitation. (D) Pie chart indicates number of genes with altered expression (≥ 2 fold-changed, $p \leq 0.05$) upon loss of IMP1 in hESCs. (E) Overlap between genes altered upon IMP1 knockdown and IMP1 eCLIP significantly bound 3'UTRs (defined as more than four-fold enriched and $p \leq 10^{-5}$ above SMInput). Bar charts only include genes profiled above minimal read depth cutoffs in both RNA-seq and eCLIP (see Methods). (F) Immunofluorescence microscopy for Phalloidin in H9 hESC following loss of IMP1, scale bar represents 10 microns. (G) Immunofluorescence microscopy for β -catenin in H9 hESC following loss of IMP1, scale bar represents 10 microns. (H) Read density plot for IMP1-enriched *CTNNB1* (β -catenin) 3'UTR, showing IMP1 (red), RBFOX2 (blue), and paired SMInput (grey) density. Clusters are indicated in boxes below. (I) Western blot and RNA-seq for *CTNNB1* following loss of IMP1 in hESCs. (J) Read density plot for IMP1-enriched *VCL* (Vinculin) 3'UTR. Dark boxes below indicate significantly enriched peaks in eCLIP relative to SMInput. Clusters are indicated in boxes below. (K) Western blot for ACTB and VCL following loss of IMP1 in hESCs. (L) ActinomycinD RNA stability assay. Expression of *ITGB1* was measured by qRT-PCR at different time points following addition of 10 μ M Actinomycin D in H9 hESCs and normalized to *PPIA* and *RPLP0*, genes determined not to change over the given time period (Error bars = mean \pm SEM, n=3).

Figure S6.

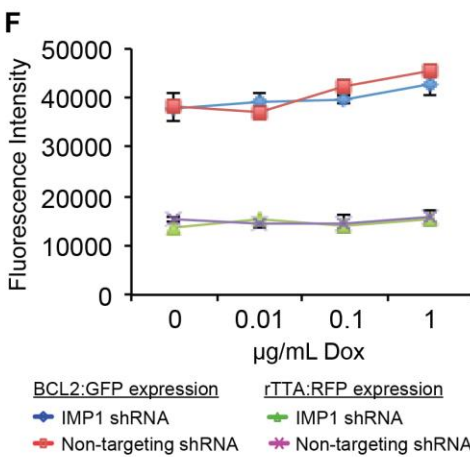
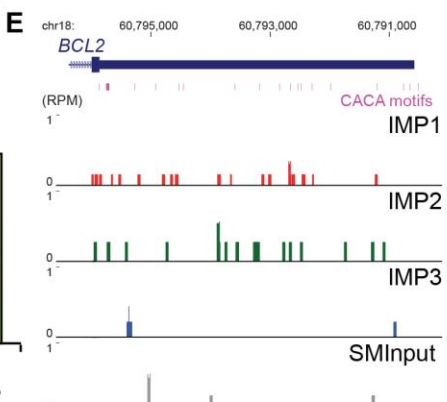
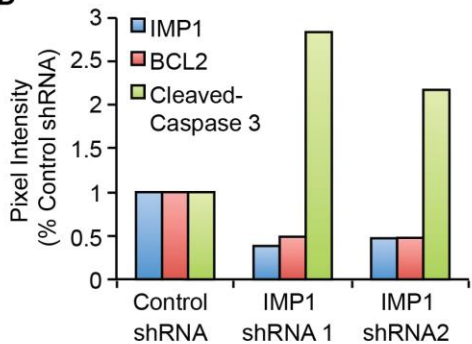
A



C



D



G

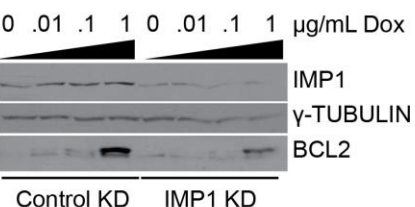


Figure S6: Related to Figure 6, IMP1 has little effect on cell proliferation but promotes cell survival through regulation of BCL2 in hESCs.

(A) Phase contrast images of HUES6 Embryoid Bodies (EBs) upon 2 weeks of undirected differentiation following transduction with lentiviruses expressing either non-targeting shRNA or shRNA targeting IMP1. Scale bar represents 1 mm. (B) KI-67 proliferation assay with non-target control and IMP1 shRNA treated cells analyzed by FACS. (left) A representative histogram is shown of untransduced, non-target shRNA treated, and IMP1 shRNA1 and IMP1 shRNA2 treated cells stained for KI-67, as well as unstained and isotype controls on untransduced cells (n=3 for each). (right) Bars indicate fraction of cells in the 'KI=67 positive' region, with error bars indicating SD. (C) Bromodeoxyuridine (BrdU) and Propidium Iodide (PI) proliferation assay with Control and IMP1^{KD} cells, analyzed by FACS. Quantification (i) and representative images of 1 biological replicate (ii-iv) are shown. Asterisks (i) represent significant differences between the control shRNA and IMP1^{KD} samples in phases G2 and S of the cell cycle (* = p < 0.05).

and ** = $p < 0.01$). Error bars indicate SD. (D) Quantitation of Western blot in Figure 6D. (E) Read density of IMP1, IMP2, and IMP3 eCLIP across *BCL2*. Overall 3'UTR signal is 2.2-fold enriched in IMP1 and 3.2-fold enriched in IMP2. (F) (top) Lines indicate expression of BCL2-copGFP in cells treated with IMP1 shRNA (blue) and control shRNA (red). Control shRNA (which targets related protein turboGFP) has 3 mismatches to copGFP, and does not show repression of copGFP. (bottom) Lines indicate cell density, using the co-transfected rTTA-RFP marker, in IMP1 shRNA (green) and non-target control (purple). Error bars = mean \pm SD, n=3. (G) Western blot of BCL2 over-expression in hESCs in the context of depleted levels of IMP1, with loading control γ -TUBULIN.

Table S1. Related to Figure 2, eCLIP sequencing library processing summary metrics.

Sample	Raw reads	Uniquely mapped reads	Unique mapping % (after repetitive element removal)	Usable reads (uniquely mapped, non-PCR duplicate)	% Usable (of uniquely mapped)	Transcript targets ($p \leq 10^{-5}$ & 4-fold enriched over SMInput)	Cluster sites CLIPper $p < 0.05$ (Remaining after removing overlapping clusters)	Stringent RBP-enriched clusters (≥ 8 -fold enriched & $p \leq 10^{-5}$ versus SMInput)
IMP1 Rep 1 H9 hESC p42	5,408,168	3,681,077	83.485%	3,524,415	95.744%	CDS: 349 3UTR: 1,264	64,845 (62,784)	1,884
IMP2 Rep 1 H9 hESC p42	6,368,699	3,498,412	78.779%	2,810,945	80.349%	CDS: 277 3UTR: 1,833	59,625 (57,648)	1,572
H9 hESC p42 Paired SMInput	17,420,962	3,030,387	57.953%	2,929,748	96.679%	-	-	-
IMP1 Rep 2 H9 hESC p43	15,564,039	7,381,368	74.527%	6,568,621	88.989%	CDS: 823 3UTR: 2,733	98,529 (95,577)	7,004
IMP2 Rep 2 H9 hESC p43	14,384,798	6,382,360	75.477%	3,744,500	58.670%	CDS: 746 3UTR: 3,314	69,146 (66,928)	4,494
IMP3 IP H9 hESC p43	13,780,206	5,043,473	71.280%	4,606,530	91.336%	CDS: 1,414 3UTR: 630	90,530 (88,164)	1,310
IgG IP H9 hESC p43	6,902,662	1,838,980	72.972%	431,079	23.441%	CDS: 1 3UTR: 5	7,888 (7,443)	142
H9 hESC p43 Paired SMInput	20,465,913	4,120,691	64.504%	4,005,777	97.211%	-	-	-
RBFOX2 IP H1 p49	3,910,870	2,038,116	69.525%	2,002,685	98.262%	CDS: 20 3UTR: 111	30,586 (29,438)	3,371
H1 p49 Paired SMInput	7,805,483	2,392,050	74.419%	1,540,208	64.389%	-	-	-

Table S3. Related to Figures 5 and 6, RNA-seq processing summary metrics.

Sample	Raw reads	Mapped reads (%)	Expressed Transcripts (RPKM ≥ 0)
Control KD A	54,210,262	42,398,504 (78%)	29,159
Control KD B	25,518,766	19,531,864 (77%)	26,090
IMP1 KD A	35,846,578	26,931,930 (75%)	27,946
IMP1 KD B	37,528,602	28,915,082 (77%)	28,391
IMP1 KD C	36,672,029	27,065,313 (74%)	27,867

SUPPLEMENTAL EXPERIMENTAL PROCEDURES

Human Illumina Bodymap Dataset Analysis

Bodymap data for 16 tissue samples from the Human Bodymap 2.0 project was downloaded from EMBL: E-MTAB-513, and H1 and HUES6 datasets were downloaded from GEO: GSE47626. H9 data shown is Rep1 of non-target shRNA RNA-seq from this study. Data was processed as described for IMP1 knockdown RNA-seq datasets. Read counting was performed using featureCounts (using the SubRead package in the R statistics software).

Antibodies Used For Western Blotting

Antibodies used were: anti-IMP1 (Cell Signaling, #2852), 1:1000; anti-IMP2 (MBL, #RN008P), 1:1000; anti-IMP3 (MBL, #RN009P), 1:1000; anti-BCL2 (BD, #610538), 1:500; anti-ITGB1 (Cell Signaling, #4706S), 1:1000; anti-ITGB5 (Cell Signaling, #4708P) 1:500; anti-HNRNPC (MBL, #RN052PW) 1:1000; anti-GAPDH (Abcam, #ab8245) 1:10,000; Cleaved-Caspase 3 (Cell Signaling, #9661), 1:500; anti-VCL (Sigma #V9131) 1:1000; anti-ACTB (Sigma, #A1978) 1:10,000; anti- β -catenin (Santa Cruz, sc-7963) 1:500; anti- γ -TUBULIN (Sigma, #T6557) 1:10,000; anti- α -TUBULIN (Abcam, #ab4074-100) 1:10,000. Western blots performed during eCLIP were done with the same antibody used for IP at 1:5000 dilution.

Nuclear/Cytoplasmic Protein Extraction

Nuclear and cytoplasmic protein extracts were isolated from 1×10^6 H9 hES cells using the NE-PER Nuclear and Cytoplasmic Extraction Reagents kit according to the manufacturer's instructions (Pierce, #78833).

Co-Immunoprecipitation of IMP Family Members in hESC

500,000 H1 hES cells were lysed (lysis buffer- 50 mM Tris-HCl pH 7.4; 100 mM NaCl; 1% NP-40; 0.1% SDS; 0.5% sodium deoxycholate with protease inhibitor (Roche cocktail)) and spun at 18,000g for 20 minutes at 4°C. Lysates were pre-cleared with anti-rabbit IgG coated Dynabeads (Life Technologies, cat#11204D). Following pre-clearing, the lysate was incubated with IMP antibody-conjugated Dynabeads (5 μ g per 200 μ l beads) overnight at 4°C (MBL #RN007P for IMP1, MBL #RN008P for IMP2 and #RN009P for IMP3). Immunoprecipitated complexes were then washed twice with 900 μ l cold High salt wash buffer (50 mM Tris-HCl pH 7.4, 1 M NaCl, 1 mM EDTA, 1% NP-40, 0.1% SDS, 0.5% sodium deoxycholate) and then with twice Wash buffer (20 mM Tris-HCl pH 7.4, 10 mM MgCl₂, 0.2% Tween-20). Samples were then resuspended in wash buffer + 10 μ l 4X NuPAGE SDS buffer + 4 μ l 1M DTT. Denaturing was performed boiling at 70°C for 10 min and samples were then loaded onto a 4-12% NuPAGE gel for Western blotting.

In Vitro Transcription and Translation of IMP Proteins in Rabbit Reticulolysates

Recombinant IMP proteins were produced using the TNT Quick Coupled Rabbit Reticulolysate System according to the manufacturer's instructions (Promega, Cat# L1170). IMP family ORFs were cloned into pRSETA (Life Technologies). 1 μ g of plasmid DNA as well as a no-template control was incubated with reaction mixture at 30°C for 90 minutes followed by Western blot for each of the IMPs using the following antibodies- (MBL #RN007P for IMP1, #RN008P for IMP2 and #RN009P for IMP3, all at 1:1000). 10% of the reaction mix was run on each lane of the gel for detection by Western blot.

eCLIP-seq Data Processing and Analysis

CLIP-seq read processing includes five major analysis steps: adapter trimming, repetitive element removal, mapping, PCR duplicate removal, and cluster identification. (1) Paired-end reads were processed with cutadapt v1.9.dev1 to remove trailing adapter sequences, resolve potential fragment dimers, and discard all reads with less than 18 high quality bases remaining. (2) To remove potential artifacts reads were first mapped to RepBase18.05 with STAR (v2.4.0i), with mapping reads discarded for further analysis. (3) Remaining reads were then mapped with STAR (v2.4.0i) to the human genome (hg19) plus annotated splice junctions. Only uniquely mapping reads were kept for downstream analysis. (4) To remove PCR duplicate reads, all reads mapping to the same position were compared based on the random-mer sequence. If more than one read mapped to the same position with the exact same random-mer (hamming distance of 0), these duplicate reads were discarded. Remaining reads are termed "usable reads". (5) Cluster identification was performed on the second read (which is enriched for termination at the protein-RNA crosslink site) using the CLIPPER algorithm (Lovci et al., 2013) which calls significantly enriched clusters independently for each gene.

To identify cluster enrichment above paired SMInput, for each cluster the number of reads mapping within that genomic region were obtained for both the IP and SMInput samples. Fold-enrichment was then calculated as the ratio of reads in IP versus SMInput, normalized by usable read depth in both experiments. Significance was determined by Yates' Chi-Square test (using the Perl Statistics::Distributions module), or Fisher's Exact Test (using the R statistics language) if the observed or expected read number in eCLIP or SMInput was below 5). If two CLIPPER-called clusters overlapped, only the cluster with the most significant enrichment above SMInput was retained.

For broad region analysis, usable (uniquely mapped, post-PCR duplicate removal) reads were counted across regions for all annotated transcripts in Gencode v19 (comprehensive). For coding genes (transcripts with the "protein_coding" transcript type), possible regions included CDS, 5'UTR, 3'UTR, and introns; for non-coding transcripts (all other transcript types), regions included

exon and introns. For each gene, a read was first queried for overlap with coding exons; then with 5'UTR or 3'UTR exons; then introns; this priority ensured that a read overlapping with CDS in one transcript and an intron in another was assigned to the CDS class only. For non-coding genes exons were similarly prioritized above introns, and coding transcripts were prioritized above non-coding. Reads were then summed across all introns or exons for the gene to obtain final region counts, and a pseudocount of 1 was added to classes for which no reads were observed. For analyses involving fold-enrichment, read counts were normalized by the total number of usable reads (RPM normalization). Only regions with at least 10 reads in one of IP or SMIInput, and where at least 10 reads would be expected in the opposite dataset given the total number of usable reads, were considered, and significance was determined by Yates' Chi-Square test or Fisher's Exact test as described above.

To generate read density plots across IMP1 peaks (Figure 3D), the midpoint was identified for each of 1884 significant enriched peaks from the first IMP1 biological replicate. Next, for each peak region in each dataset the read coverage from -300nt to +300nt flanking this midpoint was counted, and then at each position the read coverage (plus a pseudocount of 1) was divided by the sum of all points (plus pseudocounts) to generate a per-region normalization. The mean and standard error of the mean were then calculated across all remaining peak regions.

RNA Bind-N-Seq (RBNS) Full Experimental Procedures

Full length IMP1 and IMP2 were cloned downstream of a GST-SBP tandem affinity tag. The proteins were recombinantly expressed, purified via the GST tag, and the IMP1 GST tag was cleaved off with PreScission protease (GE); GST was left on for IMP2 since tag cleavage led to additional proteolysis. RBNS was performed as in (Lambert et al., 2014). Briefly, RBNS input random RNA was prepared by *in vitro* transcription using the RBNS T7 template, a DNA oligo containing a random 40mer sequence flanked by priming sites for the addition of Illumina adapters and the T7 promoter sequence. Five concentrations of RBP (5, 20, 120, 320, and 1300 nM), as well as a no RBP condition, were equilibrated in binding buffer for 30 min at 37°C. RBNS input random RNA was then added to a final concentration of 1 μM with 40 U of Superasin (Ambion) and incubated for 1 hr at 37°C. To pull down tagged RBP and interacting RNA, each RNA/protein solution was then added to 1 mg of washed streptavidin magnetic beads and incubated for 1 hr. Unbound RNA was removed from the beads, and the beads were washed once with 1 ml of wash buffer. The beads were incubated at 70°C for 10 min in 100 μl of elution buffer (10 mM Tris pH 7.0, 1mM EDTA, and 1% SDS), and the eluted material was collected. Bound RNA was extracted, reverse transcribed into cDNA, amplified by PCR, and sequenced.

RNA Bind-N-Seq Computational Analysis

Motif enrichment (R) values were calculated for k -mers ($k=4, 5, 6$) as the motif frequency in the RBP-selected pool over the frequency in the input RNA library. R values were considered significant if they had a Z-score ≥ 2 (mean and standard deviation calculated over all k -mers for each k). Values in Figure 3 are for the protein concentration library with the highest overall enrichment (320 nM for IMP1, 1300 nM for IMP2). k -mers containing “CCC”, “CUCC”, or “CACC” were removed as they are complementary to portions of the sequencing adapters flanking the random region, are enriched in multiple independent protein Bind-N-Seq experiments, and are therefore believed to be technical artifacts.

Motif logos were made from following iterative procedure on the most enriched pulldown library for $k=5$: the most enriched k -mer was given a weight equal to its enrichment over the input library ($=R-1$), and all occurrences of that k -mer were masked in both the pulldown and input libraries. All enrichments are recalculated on the masked read sets to obtain the most enriched remaining k -mer and its corresponding weight, with this process continuing until the R Z-score was less than 2. All k -mers and determined from this procedure were aligned to minimize mismatches to the most enriched k -mer, with a new motif started if the number of mismatches was greater than 2. The frequencies of each nucleotide in the position weight matrix, as well as the overall percentage of each motif, were determined from the weights of the individual aligned k -mers that went into that motif.

For comparison with CLIP-seq data, Bind-N-Seq enrichments were determined from the concentration with the largest enrichment. For enrichment in CLIP-seq 6-mers fastq sequences were extracted from all clusters, and a matched number of random clusters from the same genomic region (5'UTR, CDS, 3'UTR, proximal and distal introns, defined as 500bp from an exon intron boundary or outside that area). EMBOSS Compseq was run on the true set and background set and a delta between real and background k -mers

$$\text{was calculated with the equation: } \Delta kmer = \frac{\frac{f_{CLIP}}{N_{CLIP}} - \frac{f_{bgd}}{N_{bgd}}}{\sqrt{\left(\frac{1}{N_{CLIP}} + \frac{1}{N_{bgd}}\right) \times g \times (1-g)}}, \text{ for } g = \frac{f_{CLIP} + f_{bgd}}{N_{CLIP} + N_{bgd}}.$$

To plot enrichment, all 6-mers with the 4-mer of interest were highlighted and a KDE plot was created of all 6-mers and 6-mers that contain the 4-mer of interest. Statistical significance in differences between distributions was determined by the Kolmogorov–Smirnov 2-tailed test.

Gene Ontology Analysis

Gene Ontology annotations were obtained from ENSEMBL (5/29/15) for all annotated human genes. Significance was determined by Fisher's Exact Test (using R), with Chi-Square approximation where appropriate (using the Perl Statistics::Distributions module). Only Gene Ontology terms with at least 5 genes were considered, and Bonferroni correction was used to correct for multiple

hypothesis testing. For all comparisons, background sets were defined as all genes with sufficient read depth to be quantified (as described above).

Lentivirus Production and hESC Transduction

shRNA plasmids TRCN0000075149 (IMP1), TRCN0000255463 (IMP2), TRCN0000074675 (IMP3) were co-transfected with 3rd generation packaging plasmids into 293T cells, incubated for 2 days, and lentivirus-containing media was harvested and concentrated by ultracentrifugation. Following titration, a dilution series was performed on hESCs to determine maximum shRNA efficiency with minimal cell death; equal amounts of virus were used for all experiments. Cells were single-cell dissociated to 200k cells/sample and incubated with concentrated virus for 1 hour at 37°C at 5% CO₂ before plating out into 1 well of a 6 well plate supplemented with 10µM Rock Inhibitor Y-26732 (Calbiochem). Medium was refreshed the following day and selection with 1µg/ml Puromycin (Sigma) began 48 hours following transduction and continued for 5 days when the cells were collected for experiments unless otherwise noted in Methods. For additional IMP1 shRNAs, plasmids were co-transfected with 3rd generation packaging plasmids into 293T cells, media was changed to TESR after 24 hours, and lentiviral supernatants were collected after an additional 24 and 48 hours, pooled, and passed through a 0.45 µm filter to remove cellular debris. Following filtration and identification of the proper amount of virus to add using a dilution series, virus supernatant was added to hESCs that had been plated out at ~40% confluence using single-cell dissociation and grown overnight. Media was changed after 24 hours. For BCL2 experiments, lentiviral plasmids expressing BCL2-GFP and rTTA-RFP (#408 and #329, respectively in Ardehali et al., 2011) were obtained from the Weissman laboratory, prepared identically, and added to hESC cells previously selected for IMP1 or control shRNA transduction.

RNA-seq Preparation and Analysis

RNA was extracted as described above for three independent IMP1^{KD} biological replicates and two independent non-target control biological replicates (H9 hESC p50 for all). 1µg total RNA was treated with Ribo-zero and processed using the Tru-seq Stranded Total RNA Preparation Kit (Illumina) according to the manufacturer's instructions. Reads were adapter-trimmed, trimmed of 3' A bases, and remaining reads (\geq 18 nt long) were mapped to the human genome build hg19 using STAR (with default settings). Differential expression was identified using DEseq2 (with significance cutoffs of $p \leq 0.05$ and $\log_2(\text{fold-change}) \geq 1$, and a minimum of 10 reads in all of control or knockdown replicates required).

List of qRT-PCR primers

Gene Name	Forward	Reverse
<i>IMP1</i>	AGGCCATCGAAACTTCTCC	TTTCGGATTGAATTTCG
<i>I8s</i>	AGGCATTGACAACAGGGTTC	GTTGCACATCAGCAGCACTT
<i>GAPDH</i>	GGACTCATGACCACAGTCCATGCC	TCAGGGATGACCTGCCACAG
<i>HMBS</i>	GGCAATGCGGCTGCAA	GGGTACCCACGCGAACATCAC
<i>ACTB</i>	GCACAGAGCCTCGCCTT	GTTGTGGACGACGAGCG
<i>HNMT</i>	GGAGCTTCAAAAGTGGACT	TCTGAGATCAGGTGGTGCTG
<i>ITGB1</i>	GAGTCGCGGAACAGCAG	CAGTCCAATCCAGAAAATTGG
<i>ITGB5</i>	CCTTCTGTGAGTGCACAA	TGTAACCTGCATGGCACTTG
<i>BCL2</i>	CTGAGTACCTGAACCGCA	GAGAAATCAAACAGAGGCCG
<i>RPLP</i>	GGCGACCTGGAAGTCCAAC	CCATCAGCACACAGCCTTC
<i>PPIA</i>	GTCAACCCCACCGTGTCTT	CTGCTGTCTTGGGACCTTGT

Immunofluorescence Microscopy

Cells were rinsed with PBS, fixed in 4% paraformaldehyde in PBS at 4°C for 10 minutes. hESCs were permeabilized at room temperature for 15 minutes in 1.0% Triton X-100 in PBS. All cells were blocked in 5% donkey serum with 0.1% Triton at room temperature for 30 minutes. The following primary antibodies and dilutions were used: mouse anti-Oct4 (Santa Cruz #5279), 1:500; rabbit anti-IMP1 (Cell Signaling #2852), 1:100; rabbit anti-IMP2 (MBL #RN008P), 1:200; rabbit anti-IMP3 (MBL #RN009P), 1:200; Alexa Fluor Phalloidin 568 (Life Technologies #A12380), 1:40 per manufacturer's instructions; and mouse anti-β-catenin (Santa Cruz sc-7963), 1:100. Primary antibodies were incubated overnight at 4°C. Secondary antibodies were Alexa donkey 488, 555 and 647 anti-rabbit (Invitrogen), and Alexa donkey 488 and 555 anti-mouse (Invitrogen); all were used at 1:200. To visualize nuclei, slides were mounted with Vectashield + DAPI (Vector Labs). Images were acquired using an Olympus FluoView1000 confocal microscope at 60X.

Flow Cytometry

The AnnexinV apoptosis assay was performed using the AnnexinV-FITC Apoptosis Detection kit from BD Biosciences according to the manufacturer's instructions and analyzed using the FACS Canto II (BD Bioscience). Data was analyzed using FlowJo software. Ki-67 proliferation analysis was performed using the PE Mouse Anti-Human Ki-67 Set (BD #556027), according to the manufacturer's instructions on the FACSCanto II. Data was analyzed using FlowJo software. Significance was determined by unpaired *t*-test between the control shRNA sample and IMP1 shRNA samples (N = 3 for each).

Embryoid Body (EB) Differentiation

HUES6 hESCs transduced with lentiviruses expressing either a non-targeting shRNA (SHC002) or shRNA targeting IMP1 (TRCN0000075149) were treated with collagenase until the edges were detached from the plate (1mg/ml concentration, ~90minutes) then detached with a cell scraper, rinsed, and resuspended in EB medium (DMEM/F12 containing 10% FBS, 0.5 mM L-glutamine, 0.1 mM non-essential amino acids and 55 µM β-mercaptoethanol). EBs were maintained on low-attachment 6 well plates and replenished with fresh EB media approximately every 3 days for two weeks.

BRDU Cell Cycle Analysis

For BRDU cell cycle analysis, cells were incubated in mTeSR1 containing 10 µM BrdU for 30 minutes. Cells were dissociated using Accutase (Innovative Cell technologies, Inc), rinsed with PBS and fixed in 70% ethanol overnight at 4°C. The cell pellet was resuspended in ice cold 0.1 M HCl/0.5% TritonX-100 for 10 minutes, after which the cells were boiled for 10 minutes in a water bath and transferred to ice for 5 minutes to cool. After a brief incubation in 0.5% Triton-X100 in PBS, cells were incubated with a rat-anti-BrdU antibody (1:100 dilution; Axyll #OBT0030) for 30 minutes followed by incubation with an Alexa 488 goat anti-rat secondary antibody (1:200; Life Technologies) for 20 minutes. The cell pellet was resuspended in PBS containing 5 µg/ml of Propidium Iodide and 100 µg/ml of RNaseA. Analyses were conducted using a FACScan (BD Bioscience) and data was analyzed using FlowJo software. Significance was determined by unpaired *t*-test between the Control sample and IMP1 KD sample.

In Vitro Transcription of RNAs Used in EMSA

To produce RNAs by *in vitro* transcription, single stranded DNA oligos corresponding to the RNAs of interest and containing the T7 promoter were first annealed to the second strand of the T7 promoter by heating at 95°C and then cooling on benchtop to room temperature, followed by *in vitro* transcription using the MEGAshortscript T7 Kit according to the manufacturer's instructions (Ambion #AM1354M). Transcribed RNAs were then cleaned up using the MEGAclear Transcription Clean Up kit according to the manufacturer's instructions (Ambion #AM1908) with the exception of the *ACTB* truncated RNA which was LiCl precipitated due to the short length. CIP treatment (Antarctic phosphatase, NEB #M0289S) followed by phenol-chloroform extraction and ethanol precipitation was performed to remove residual contaminants. PNK treatment (NEB) and 5' end labeling with [γ^{32} P]-ATP (PerkinElmer) was performed for 20minutes at 37°C followed by clean up on Illustra MicroSpin G25 spin columns (GE Healthcare). Purified RNAs were then quantified using a scintillation counter. 32 P-labeled 3'UTR target RNAs used in the experiment were as follows: *ACTB* 3'UTR zipcode WT (88bp) - 5'-

CCUCCAUCGUCCACCGCAAAUGCUUCUAGGCGGACUAUGACUUAGUUGCGUUACACCUUUUCUUGACAAAACCU
AACUUGCGCAGAAA -3' (human zipcode noted in bold); Truncated *ACTB* zipcode (26bp) - 5' –
UGUGAUGAAACAAACCAUAAAUGC - 3' (nucleotides 29-54 from Chao et al., 2010); *BCL2* 3'UTR WT (88bp) - 5'-
AAUGACCAGCAGAUCAAUCUAUGGUGGUUGACCUUUAGAGAGAUUGCUUUACGUGGCCUGUUCAACACAGA
CCCACCCAGAGCCC -3'; Mutated *BCL2* 3'UTR (88bp), bold sequence inverted and mutated (underlined portion is mutated) - 5'-
AAUGACCAGCAGATTCAAUCUAUGGUGGUUGACCUUUAGAGAGAUUCCCGAGACCCACCCCAGAGAGAACUUUG
UCCGGTGCAUUUCG -3'.